Research Article

High-Entropy Oxides: A New Frontier in Photocatalytic CO_2 Hydrogenation

Dalibor Tatar, Habib Ullah, Mohit Yadav, Jelena Kojčinović, Stjepan Šarić, Imre Szenti, Tina Skalar, Matjaž Finšgar, Mi Tian, Ákos Kukovecz, Zoltán Kónya, András Sápi,* and Igor Djerdj*

Cite This: ACS Appl. Mater. Interfaces 2024, 16, 29946−29962

Read Online

ACCESS | Metrics & More | Article Recommendations | Supporting Information

ABSTRACT: Herein, we investigate the potential of nanostructured high-entropy oxides (HEOs) for photocatalytic CO_2 hydrogenation, a process with significant implications for environmental sustainability and energy production. Several cerium-oxide-based rare-earth HEOs with fluorite structures were prepared for UV-light driven photocatalytic CO_2 hydrogenation toward valuable fuels and petrochemical precursors. The cationic composition profoundly influences the selectivity and activity of the HEOs, where the $Ce_{0.2}Zr_{0.2}La_{0.2}Nd_{0.2}Sm_{0.2}O_{2-\delta}$ catalyst showed outstanding CO_2 activation (14.4 mol_{CO} kg_{cat}^{-1} h^{-1} and 1.27 mol_{CH_3OH} kg_{cat}^{-1} h^{-1}) and high methanol and CO selectivity (7.84% CH_3OH and 89.26% CO) under ambient conditions with 4 times better performance in comparison to pristine CeO_2. Systematic tests showed the effect of a high-entropy system compared to midentropy oxides. XPS, *in situ* DRIFTS, as well as DFT calculation elucidate the synergistic impact of Ce, Zr, La, Nd, and Sm, resulting in an optimal Ce^{3+}/Ce^{4+} ratio. The observed formate-routed mechanism and a surface with high affinity to CO_2 reduction offer insights into the photocatalytic enhancement. While our findings lay a solid foundation, further research is needed to optimize these catalysts and expand their applications.

KEYWORDS: ceria, high-entropy oxides, photocatalytic CO_2 hydrogenation, selectivity, DFT
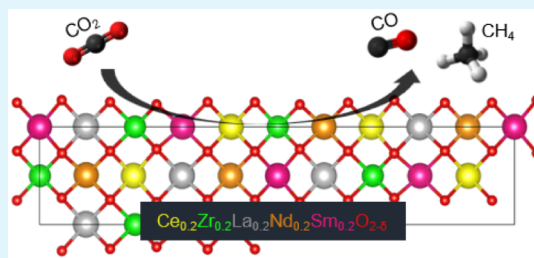
1. INTRODUCTION

Carbon dioxide (CO_2) is a double-edged sword. Although it contributes to creating a warm environment on Earth, the excessive burning of fossil fuels has led to a continuous rise in CO_2 concentration in the atmosphere, resulting in irreversible climate changes.[1] In order to reduce the amount of CO_2 in the atmosphere, methods which include CO_2 capture, storage, and chemical utilization are used.[2] Highly efficient catalysts are necessary to reduce the energy required for converting CO_2 to less harmful chemicals.[3] The desired outcome is to convert CO_2 into products with high selectivity according to the specific application requirements. The most likely products for different types of atmospheric pressure hydrogenation reaction (thermocatalytic, photocatalytic, etc.) are carbon monoxide (CO) and methane (CH_4) through reverse water−gas shift and Sabatier reaction, respectively.[2,4] CO can be further transformed into chemicals and fuels through established gas conversion technologies, such as Fischer−Tropsch synthesis and methanol synthesis.[5,6]

In its early stages, photocatalytic CO_2 conversion shows great promise as a clean technology for reducing greenhouse gas emissions.[7] This process usually involves a semiconductor photocatalyst that absorbs light and converts CO_2 through various pathways, resulting in different products.[8,9] However, for a successful photocatalytic CO_2 conversion to occur, the photocatalyst must possess qualities such as an appropriate bandgap, band structure, and long-life charge carriers with optimal mobility.[10] While there are already photocatalysts available,[11,12] continuous exploration for highly effective materials is crucial to achieve practical application.[13]

Entropy materials are categorized based on the disorder in element arrangement within their lattice structures. The configurational entropy of multielement oxides can be calculated using Boltzmann's entropy equation,[14] where R is the molar gas constant. Low-entropy oxides ($S_{config} < 1R$) exhibit minimal disorder, while medium-entropy oxides ($1R < S_{config} < 1.5R$) and high-entropy oxides ($S_{config} > 1.5R$) show increasing disorder. In terms of element number, medium-entropy oxides comprise more than two but less than five components, while high-entropy oxides have a minimum of five components. The study of high-entropy materials has emerged as a rapidly growing and dynamic field within material science. These materials, consisting of a mixture of various elements in single-phase compounds, are known for their unique properties and crystal
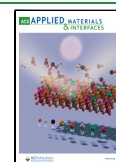
Table 1. List of Synthesized High−Entropy Compounds Together with Elements Used for the Synthesis of HEOs

compound name	chemical formula	element	coordination	charges	ionic radii
CZLPY	$Ce_{0.2}Zr_{0.2}La_{0.2}Pr_{0.2}Y_{0.2}O_{2-\delta}$	Ce	VIII	+3/+4	1.143/0.97
CZLNS	$Ce_{0.2}Zr_{0.2}La_{0.2}Nd_{0.2}Sm_{0.2}O_{2-\delta}$	Zr	VIII	+4	0.84
CZLPN	$Ce_{0.2}Zr_{0.2}La_{0.2}Pr_{0.2}Nd_{0.2}O_{2-\delta}$	La	VIII	+3	1.16
CZLPS	$Ce_{0.2}Zr_{0.2}La_{0.2}Pr_{0.2}Sm_{0.2}O_{2-\delta}$	Pr	VIII	+3/+4	1.126/0.96
CZLNY	$Ce_{0.2}Zr_{0.2}La_{0.2}Nd_{0.2}Y_{0.2}O_{2-\delta}$	Nd	VIII	+2/+3	1.29/1.109
CZLSY	$Ce_{0.2}Zr_{0.2}La_{0.2}Sm_{0.2}Y_{0.2}O_{2-\delta}$	Sm	VIII	+2/+3	1.27/1.079
		Y	VIII	+3	1.019

structures due to their high configurational entropy.[15] The discovery of high-entropy oxides (HEOs) has generated significant interest in the scientific community, particularly due to their ability to incorporate five or more different cations into a single-phase oxide system.[15] The key step for creating a single-phase high-entropy material is in selecting metal cations with similar ionic radii, oxidation state, and coordination number.[15] These materials are of great interest due to their versatility and ability to be adjusted, making them useful in various applications such as energy conversion and storage,[16] hydrogen and oxygen production,[17] and heterogeneous catalysis.[13,18] Despite the progress made in this field, there are still unexplored combinations of elements and potential applications that offer promising opportunities for future research and development.

Nanostructured ceria (CeO_2) finds application across various fields of scientific researches in the last decades, due to its accessibility, cost-effectiveness, stability, durability, high surface area of ceria nanoparticles, etc.[19] Due to these advantageous properties of CeO_2 it has been found to have a potential as a photocatalyst for a range of purposes, including producing energy, generating hydrogen, releasing oxygen, and improving storage capacity. Its redox potential also makes it possible to convert cerium easily between Ce^{4+} and Ce^{3+} and generate oxygen vacancies, which can be further enhanced through doping effect.[20] By alteration of its physical and chemical properties, ceria becomes an even more viable option for these applications. Defects, particularly oxygen vacancies, play a crucial role in boosting ceria's photocatalytic properties.[5,21] Investigation of ceria-based high-entropy oxides is important due to their potential for enhanced properties compared to traditional oxides. Incorporating elements like Zr or rare earth elements into ceria-based compositions has shown potential in improving catalytic and mechanical properties. Understanding how incorporation of other elements affects material properties can lead to the development of more efficient materials for various applications.

In our research, we have synthesized six ceria-based high-entropy oxides with a fluorite-type structure and average particle sizes in the range of 4−5 nm. Their efficiency in converting CO_2 into products through photocatalysis was further evaluated. The synthesis process followed an environmentally friendly and low-cost sol−gel citrate method that had previously been utilized in the preparation of high-entropy oxides[22,23] and perovskite oxides.[24] To better understand the photocatalytic behavior, thorough structural analysis and surface studies were conducted. A catalytic activity of the oxides was *in situ* studied with the aim to discover the mechanism behind CO_2 hydrogenation. In addition, density functional theory (DFT) simulations have been performed to explore how a complex oxide catalyst (HEO) can aid in the reduction of CO_2. Our DFT analysis identified Zr as the crucial element in this process, directing the reduction of

CO_2 on the surface of HEO catalysts. Through DFT simulations, we observed the accumulation of charges at the Zr sites of HEO catalysts, facilitating the subsequent transfer of electrons from the catalyst to the CO_2 molecules. Notably, this electron transfer phenomenon exclusively occurs at the Zr sites. This electron transfer activates CO_2, initiating the reduction process. This is a vital step toward utilizing CO_2 as a resource, instead of treating it as waste.

Our motivation for investigating the photocatalytic CO_2 hydrogenation of high-entropy oxide compounds was based on our previous successful research in which we used HEOs as photocatalysts for water purification from AZO dyes.[22] Furthermore, as part of the same research, we used HEOs as electrocatalysts for the hydrogen evolution reaction, and they demonstrated remarkable hydrogen production. These promising results prompted us to investigate the potential of HEOs as photocatalysts for CO_2 hydrogenation. The ability of HEOs to exhibit exceptional catalytic activity for various applications suggests that they have a unique atomic-level structure that allowsenhanced catalytic activity. Hence, exploring the CO_2 hydrogenation activity of HEOs could offer new insights into the development of highly efficient catalysts for sustainable energy conversion.

2. EXPERIMENTAL SECTION

2.1. Materials. For the synthesis of HEOs, commercially available chemicals were purchased and used without further purification. Chemicals were purchased from Sigma-Aldrich, Germany (cerium(III) nitrate hexahydrate (99.9%), zirconium(IV) oxynitrate hydrate (99.9%), lanthanum(III) nitrate hexahydrate (99.9%), praseodymium-(III) nitrate hexahydrate (99.9%), neodymium(III) nitrate hexahydrate (99.9%), samarium(III) nitrate hexahydrate (99.9%)), Alfa Aesar, Germany (yttrium(III) nitrate hexahydrate (99.9%)), T.T.T., Croatia (citric acid monohydrate (99.9%)), and Gram − Mol, Croatia (concentrated ammonia solution 25%).

2.2. Preparation of Compounds. The list of synthesized HEOs along with structural features[25] for each metal cation is presented in Table 1. High-entropy oxide nanoparticles were synthesized using a modified sol−gel citrate method.[22,26]

An equimolar composition of 0.2 mmol of each element was chosen to achieve the maximum configurational entropy of the system. The synthesis procedure involved dissolving 0.2 mmol of each metal nitrate in a 10% citric acid solution (previously prepared by dissolving 10 g of citric acid in 100 mL of Milli-Q water). The solution was stirred constantly and concentrated ammonium solution was added dropwise to achieve a pH of approximately 5 (pH-meter 211, HANNA, Croatia). The solution was kept under constant stirring and heated to 120 °C until all of the liquid evaporated, forming a black resin. The black resin was further dried in an oven (Instrumentaria ST−01/02, Croatia) at 120 °C for 24 h, then ground in a mortar, with a pestle, and calcined at 700 °C for 8 h using a muffle furnace (LT5/11/B410, Nabertherm, Germany) with a heating rate of 4 °C per minute. This resulted in the formation of single-phase high-entropy stabilized oxide catalysts.

2.3. Structural and Spectroscopic Characterization. The crystal structure and microstructure of the synthesized materials were
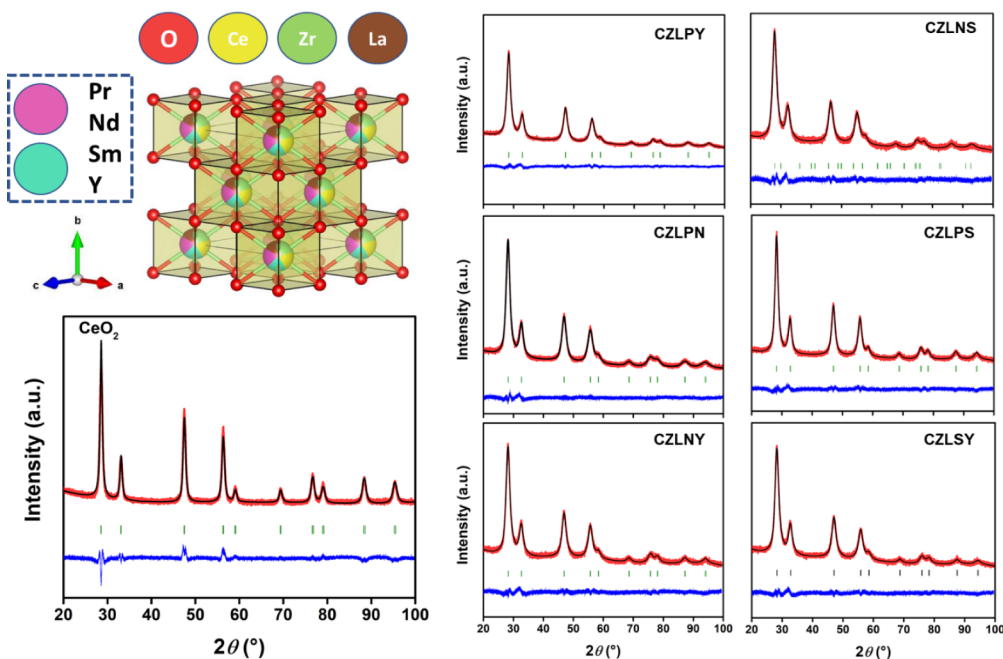
Figure 1. Rietveld plots of the investigated synthesized HEO catalysts and pure CeO_2, accompanied by the visualized fluorite-type crystal structure.

analyzed by using X-ray powder diffraction (XRD), utilizing a PANalytical Aeris diffractometer (Malvern PANalytical, UK) with a Cu Kα radiation source (at 40 kV and 15 mA). The XRD analysis was performed at 298 K with a step size of 0.02 and 1° divergence slit. The PXRD patterns were analyzed using the FULLPROF software[27] and the Rietveld refinement method. The Rietveld refinement was performed with the purpose of extracting and quantifying important structural and microstructural information. The structures were visualized using the VESTA software.[28] The UV−vis spectra and optical bandgap were determined using a solid-state UV/vis/NIR spectrophotometer (UV-3600Plus, Shimadzu, Japan). To study the thermal stability and potential phase changes of the catalysts at high temperatures, a thermogravimetric analyzer/differential scanning calorimeter (TGA/DSC System 1, Mettler Toledo, USA) was utilized over a temperature range of 25 to 1000 °C with a heating rate of 10 °C/min in an O_2 atmosphere. The infrared spectroscopy analysis was conducted using a Shimadzu FTIR-8400S spectrometer (Shimatzu, Japan). The N_2 physisorption measurements were performed by using the Quantachrome NOVA 3000e instrument at a temperature of liquid N_2. To prepare the compound for adsorption measurements, it was subjected to vacuum at a temperature of 250 °C for 5 h to remove any unwanted impurities. The surface structure was examined using a Thermo Fisher Scientific Apreo C scanning electron microscope (Thermo Fisher Scientific, Waltham, MA, USA). A field emission scanning electron microscope (FE-SEM, Zeiss ULTRA Plus, Zeiss, Germany) was used to collect images in the secondary electron image, using an InLens detector at a cathode voltage of 20 kV and an approximate working distance (WD) of 5.5 mm. The dried powder compounds were mounted on aluminum stubs by double-sided carbon conductive tape. Prior to imaging, they were coated with a ca. 10 nm thick conductive Au/Pd layer using a high sputter coater (Quroum Q150T ES, UK). Mapping was performed on an Oxford Instruments microanalysis system consisting of a 50 mm² silicon drift detector (X-Max50, Oxford Instruments plc, Tubney Woods, Abingdon, UK). The results of element distributions (element maps) were processed using Inca (Oxford Instruments, UK) software. As-synthesized catalysts were characterized using a Tecnai G² 20 X-Twin (FEI Company, Hillsboro, OR, USA) high-resolution transmission electron microscope (HR-TEM), equipped with electron diffraction, and operated at a high voltage (200 kV). All microscopy images were analyzed using ImageJ software.[29]

XPS measurements were performed with a Supra+ instrument (Kratos, Manchester, UK) using the Al K$_\alpha$ X-ray excitation source and a charge neutralizer that was on during the measurements. The angle between the surface of the compound and the path of the electrons to the analyzer was 90° (take-off angle). High resolution and survey spectra were measured at 20 and 160 eV pass energy, respectively. The powder compounds were attached to carbon tape, which was placed on the Si wafer. XPS measurements and data processing were performed by using ESCApe 1.5 software (Kratos). The binding energy scale was corrected using the C−C/C−H peak at 284.8 eV in the C 1s spectra. The background of the peaks was determined with a Shirley background correction.

2.4. Photocatalytic Test. The study aimed to investigate the photoreduction activity of the compounds by conducting the photocatalytic hydrogenation of CO_2 in a flow microreactor. The microreactor consisted of an inner glass cylinder (d_{inner} = 6.4 cm, h = 25 cm) and an outer glass cylinder (d_{inner} = 10.2 cm, h = 25 cm). The smaller glass cylinder contained an 11 W UV lamp (λ = 370 nm). The catalysts were immobilized on the outer surface of the smaller glass cylinder by suspending 250 mg of the catalyst in a few mL of absolute ethanol using ultrasonication. The immobilized catalysts were pretreated by introducing various gases (Ar for 20 min, O_2 for 30 min, Ar for 10 min, and H_2 for 10 min, in that order) into the space between the cylinders while heating the inner cylinder to 250 °C using a heating rod. A gas mixture of CO_2 and H_2 (at a ratio of 1:2) was then introduced into the space between the cylinders by using an Aalborg mass flow controller (Hazel Park, MI, USA). To analyze the products, a fixed amount of the CO_2/H_2 gas mixture was recirculated between the reactor and a gas chromatograph (GC) by using a gas pump. The reactants and products were separated by passing them through a 2-meter-long capillary column (d = 0.635 cm) packed with a Porapak QS polymer (Bellefonte, PA, USA) and detected using a thermal conductivity detector and a flame ionization detector. The products were analyzed using a HP 5890 Series II GC.

DRIFTS analysis was performed by using an Agilent Cary 670 FTIR spectrometer (Agilent, CA, USA) equipped with a Harrick Praying Mantis diffuse reflectance attachment. To prepare the catalysts for testing, we followed the pretreatment conditions as in the experiments but used helium as an inert gas instead of argon. After pretreatment, background spectra were recorded. CO_2/H_2 mixture with a ratio of 1:2 was introduced into the DRIFTS cell at room temperature, along with a stream of helium (He) in a flow rate of 40 mL/min. The catalyst was
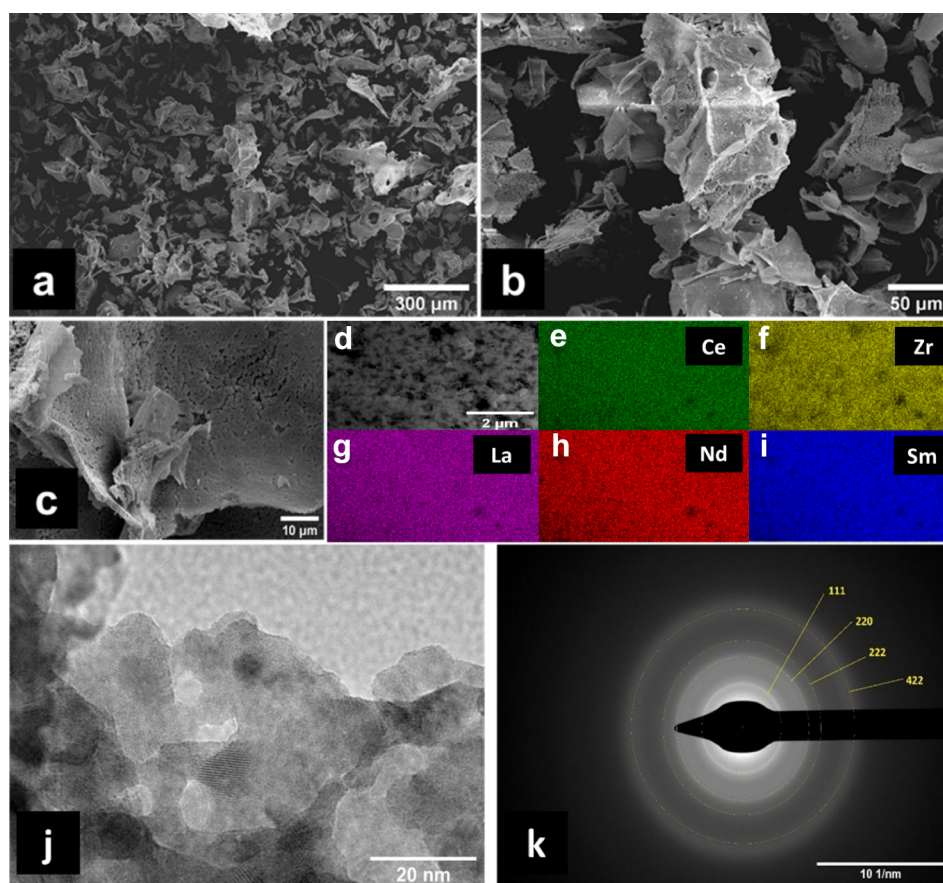
Figure 2. (a−d) SEM images under low and high magnification of the CZLNS catalyst; (e) SEM image under high magnification used for EDS mapping; (f−i) Elemental maps of the CZLNS catalyst; (j,k) HRTEM images of the CZLNS compound along with the SAED image.

gradually heated from room temperature to 250 °C at a heating rate of 10 °C/min. The spectra at an interval of 50 °C were recorded. The spectral data were collected within the range of 4000 to 800 cm^{-1} with a resolution of 2 cm^{-1}.

2.5. Density Functional Theory (DFT) Simulations. All density functional theory (DFT) calculations were conducted using Quantum-ATK, and the results were visualized using VNL (Version 2019.12).[30] A cubic unit cell of ceria (CeO_2) with a space group $Fm-3m$ and lattice parameter $a = 5.467$ Å was used to represent the experimentally prepared HEO compounds, as per literature data.[22] To accommodate doping, a $1 \times 5 \times 1$ supercell of CeO_2 was employed to construct models containing dopants. The local density approximation (LDA) and Perdew−Zunger (PZ) were utilized as exchange and correlation functionals, respectively, in conjunction with Fritz−Haber−Institute (FHI) pseudopotentials and a double Zeta polarized basis set. Electronic properties such as the density of states (DOS), effective potential, electron difference density (EDD), electrostatic difference potential (EDP), and electron localization functional (ELF) were simulated by using the same method. The linear combination of atomic orbitals (LCAO) method was applied for Ce, Zr, La, Pr, Y, Nd, Sm, O, C, and H atoms. A $3 \times 3 \times 1$ Monkhorst−Pack k-grid with an energy cutoff of 75 hartree was used for the slabs.

3. RESULTS AND DISCUSSION

3.1. X-Ray Diffraction. The phase purity, crystal structure, and microstructural features of newly synthesized HEOs were initially studied by using powder X-ray diffraction (PXRD). The obtained XRD powder patterns are displayed in Figure S1, and they reveal that all synthesized catalysts exhibit phase purity at least until the resolution limit of XRD technique. The Rietveld refinement plots that are displayed in Figure 1 further

corroborate the phase purity and point to the fluorite structure of ceria that crystallized in the cubic $Fm-3m$ space group. The structural features obtained from the Rietveld refinement are presented in Table S1. The microstructural size-microstrain analysis shows an average crystallite size of 4−5 nm for high-entropy compounds, while for pure CeO_2, the average crystallite size is slightly larger and it amounts to 11 nm. The lattice parameters and unit cell volume increase with the addition of cations compared to pure CeO_2 which provides evidence for their successful incorporation into the host CeO_2 lattice. The mutual variation of lattice parameters among the studied HEOs depends on the ionic radii of cations, with evident expansion of the crystal lattice due to the incorporation of cations larger than Ce. The crystal structure shown on the top left part of Figure 1 reveals a fluorite-type structure consisting of a face-centered cubic unit cell of cations, with oxygen anions occupying the tetrahedral interstitial sites. Five different rare-earth metal cations alternate randomly at crystallographic site 4a making this structure disordered. These cations are coordinated by eight nearest-neighbor oxygen anions, while each oxygen anion is coordinated by four nearest-neighbor metal cations.

In high-entropy materials, lattice defects mostly originate from the lattice strain due to the mismatch of different constitutive metal cations. Such defect sites might tune the electronic structure of the active sites, facilitating the photo-catalytic CO_2 reduction. Such feature should be detectable by the increased value of XRD-derived lattice microstrain. Indeed, in this consideration, all obtained microstrain values of HEOs (Table S1) are significantly larger in comparison with pure

CeO_2. It is noteworthy that the CZLNS compound ($Ce_{0.2}Zr_{0.2}La_{0.2}Nd_{0.2}Sm_{0.2}O_{2-\delta}$) exhibits by far the largest value of lattice microstrain among all studied HEOs, making it somehow special.

3.2. Electron Microscopy Study. The morphology and composition of the studied compounds were investigated by using scanning electron microscopy (SEM) coupled with energy dispersive X-ray spectroscopy (EDS). The high-entropy compounds displayed flake-like morphology with visible porosity (Figures 2a–d and S2). Higher magnification SEM images reveal that the flakes are thin nanosheet-like structures. The EDS analysis was used to evaluate the elemental composition, homogeneity, and weight distribution of elements in the HEOs, demonstrating a uniform distribution of the elements within the high-entropy compounds. Figure 2 displays SEM images at different magnifications and corresponding elemental maps of selected high-entropy compound CZLNS. The EDS data (and sum spectrum for CZLNS in Figure S3) confirmed that the empirical formula of all compounds was relatively close to nominal $Ce_{0.2}Zr_{0.2}La_{0.2}X_{0.2}Y_{0.2}O_{2-\delta}$ (X, Y = Pr, Nd, Sm, Y), as shown in Table S2.

High-resolution transmission electron microscopy (HR-TEM) was further utilized to validate the local crystallinity at the nanoscale level. HR-TEM image shown in Figure 2j reveals that the nanoparticle sizes of the CZLNS compound align with the data obtained from the Rietveld analysis, which revealed the presence of crystallites with an average size of 4 nm. HR-TEM analysis was performed for all studied HEO compounds, along with the parent CeO_2, as shown in Figure S4, and no deviation from the data obtained by the Rietveld analysis was observed. All accompanied selected area electron diffraction (SAED) patterns exhibit well-resolved Debye–Scherrer rings which are typical for nanocrystalline materials, as shown in Figures 2k and S4.[31] SAED patterns were indexed to the cubic $Fm-3m$ space group, confirming XRD results.

3.3. Physisorption Measurements. The results of the physisorption measurements conducted on all catalysts using nitrogen as an adsorptive at 87 K are shown in terms of adsorption–desorption isotherms in Figure S5, while extracted numerical data are displayed in Table S3. All of the studied HEOs exhibited type IV isotherm characteristic for mesoporous materials. The pore sizes of all catalysts were found to be similar, falling within the range of 10.7 to 14 nm in diameter, indicating that the catalysts have similar pore structures. Furthermore, all catalysts displayed specific pore volumes ranging from 0.06 to 0.12 $cm^3 g^{-1}$ and a specific surface area ranging from 21 to 36 $m^2 g^{-1}$. It is worth noting that the compounds lacking praseodymium exhibited larger surface areas, pore volumes, and pore size diameters compared to those containing praseodymium. This could be attributed to the tendency of praseodymium 3+ ions in Pr-HEO to undergo advanced sintering, leading to a partial collapse of the nanoscale porosity.[22] As a result, the presence or absence of praseodymium may impact the porosity of the compounds and subsequently influence their properties.

3.4. Thermal Stability. The thermal stability of catalysts was determined by using thermogravimetric analysis (TGA) and differential scanning calorimetry (DSC). The stability of all synthesized HEOs was examined within a temperature range of 25 to 1000 °C, at a heating rate of 10 °C per min. The results, presented in Figure S6, indicate that all HEOs are stable and showed no further weight loss in the temperature range studied. This confirms the stability of the compounds after calcination

and suggests that they could be used at high temperatures to avoid damage to the materials. A slight loss of nearly 1 wt % for all compounds is attributed to the loss of surface moisture. DSC curves of all compounds show no evidence of phase changes, corroborating the phase stability of prepared catalysts in the studied temperature range. Upon heating the prepared catalysts under an oxygen atmosphere, its uptake was observed, which confirms the presence of oxygen vacancies in the materials. These vacancies are known to influence the catalytic activity of the materials by facilitating the adsorption and activation of CO_2 molecules. The enlarged TGA curve of studied catalysts can be divided into 3 temperature regions, as shown in Figure 3.
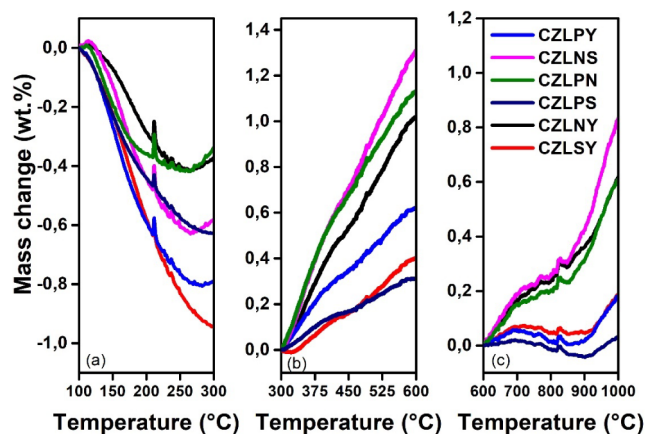

Figure 3. TGA curves of as-synthesized high-entropy compounds in temperature ranges: a) 100–300 °C, b) 300–600 °C, and c) 600–1000 °C heated in an oxidative atmosphere (O_2, 200 mL/min) and heating rate 10 °C/min.

The first region, 100–300 °C, shows a mass decrease of 0.3% up to almost 1% (Table S4). This could be due to the removal of adsorbed species at the surface of as-synthesized compounds. There are also peaks for each compound in the range of 200–215 °C that point to quick mass increase–decrease behavior. This change could be attributed to CO_2 desorption from the surface of catalysts.[32] The second region 300–600 °C shows a mass increase trend of 0.3 up to 1.3 wt %, which is obviously attributed to the oxygen uptake that fills surface oxygen vacancies resulting in the oxidation of surface cations, such as Ce^{3+} and Pr^{3+}. It is noteworthy that the largest mass change of 1.3 wt % is recorded for catalyst CZLNS, which has the largest quantity of surface adsorbed oxygen species (70.9 wt % as-synthesized) as deduced by XPS and will be further elaborated below. The third region, 600–1000 °C, shows a slight increase in the mass of as-synthesized compounds, attributed to further oxidation. There are small peaks in the range of 750–850 °C that also show mass increase–decrease behavior. This range is where surface carbonates are probably decomposed[24] and carbonate-free cations are oxidized.

3.5. Spectroscopy. *3.5.1. Fourier-Transform IR Spectroscopy.* After calcination, the HEOs were further analyzed by Fourier transform IR spectroscopy. The stacked spectra are displayed in Figure S7 and show the presence of significant absorption bands at 3568 and 3280 cm^{-1}, indicating O–H stretching and bending, respectively, of O–H from water molecules that are present on or adsorbed onto the surface, also corresponding to TGA analysis. Two bands at 2360 and 2336 cm^{-1} were assigned to environmental CO_2 molecules because

the FTIR sample holder was not sealed, while the bands appeared at 1494 and 1399 cm^{-1} are attributed to the carbonate groups that were most probably formed by CO_2 adsorption on the catalyst surface.[33] This follows from the absence of any metal-carbonate phases which might be detected by XRD. The bands at lower wavenumbers (under 600 cm^{-1}) originate from metal-oxygen stretching vibrations.

3.5.2. UV−Vis Spectroscopy and Optical Bandgap Calculation. The synthesized HEOs displayed variations in their color, and each compound appears in a different shade of brown (compounds containing praseodymium) or white (compounds without praseodymium). These color variations highlight differences in the optical behavior of the compounds and can be attributed to the synergistic interaction of multiple components within the high-entropy oxide system. The normalized absorbances of the as-synthesized HEOs were obtained by transforming the room-temperature reflectance spectra through the Kubelka−Munk function and are displayed in Figure 4. It is clear that the recorded UV−vis spectrum of pure
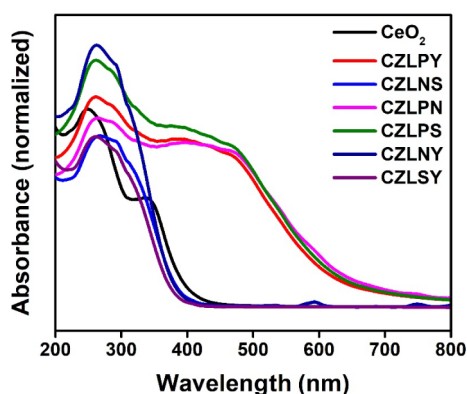
Figure 4. Normalized absorption spectra for all synthesized compounds obtained by transformation of reflectance spectra by the Kubelka − Munk function.

CeO_2 and CeO_2-based HEOs exhibits two absorption bands that are observed in the UV region for pure CeO_2 at 340 and 250 nm, while for HEOs at 295−298 and 258−261 nm.

Generally, the absorption of ceria in the UV region occurs at about 255, 285, and 340 nm.[34] The former maxima (255 nm) correspond to the O^{2-} to Ce^{3+} charge transfer transitions, whereas the latter two absorption maxima may be caused by the O^{2-} to Ce^{4+} charge transfer (285 nm) and interband (340 nm) transitions. Pr-contained HEOs show the shift of adsorption edges toward the longer wavelength into the visible region, i.e., red shift, which indicates a narrowing of optical bandgaps. From the reflectance spectra (Figure S8), optical bandgaps were extracted assuming a direct allowed transition from the Tauc plot: $(F(R)h\nu)^2-h\nu$ plot, where $h\nu$ is the incident photon energy (in eV) and $F(R)$ is the Kubelka−Munk function (insets of Figure S8). The optical bandgaps of the synthesized catalysts are summarized in Table S5. Lower bandgap values are found for Pr-containing HEOs (CZLPY, CZLPN, and CZLSY) in accordance with the extension of absorption edges into the visible light region, which is caused by the modification in the electronic structure of Pr-containing HEOs compared to pure ceria. The conduction band in pure ceria is composed mainly of Ce 4f states with a slight admixture of the O 2p states (due to hybridization). However, incorporation of Pr cations in the CeO_2 host lattice introduces conduction bands to the bottom of

ceria, Pr 4f states that modify bandstructure (DOS) of conduction band, causing its shift toward the top of the valence band and a narrowing bandgap as evidenced from our previous studies.[35−37] Doping ceria with other elements such as Zr, La, Nd, Sm, and Y can have a significant impact on its bandgap value.[38] The size and charge of these dopant ions can introduce defects and modify the electronic structure of ceria, leading to a wider or narrower bandgap. Ceria-based high-entropy oxides (HEOs) have been found to exhibit lower bandgap values than pure ceria, which is evident comparing Table S5 and Figures S8 and S9.

The diffuse reflectance spectra (Figure S8) in the visible light region demonstrate similar patterns for CZLNS and CZLNY compounds, i.e., similar sharp and well-defined absorption strengths for the peaks that were assigned to Nd^{3+} absorptions.[35,37,39] The absorption features of Nd in UV−Vis reflectance spectra originate from the f−f electron transition of Nd^{3+}. The absorptions are sharp because the Nd 4f orbitals are shielded from outer orbitals, reducing the effects of crystal fields when Nd is in crystal coordination.[40] Even though the CZLPN compound contains Nd in equal amounts as CZLNS and CZLNY, reflectance UV/vis spectra show only one absorption peak typical for Nd^{3+} at 750 nm.

3.5.3. X−ray Photoelectron Spectroscopy. Figure S10 shows C 1s spectra with four deconvoluted peaks. The peaks for C−C/C−H, C−O, and COO/COOH containing species most likely originate from adventitious carbonaceous species adsorbed on the surface after sample preparation and transfer to the spectrometer. The C 1s peak at the most positive binding energy corresponds to the carbonates. The decrease in the amount of carbonates follows the trend of CZLNY > CZLNS ≈ CZLSY > CZLPN ≈ CZLPS > CZLPY. This decrease can be attributed to the reduction of surface carbonates along with the reduction of CO_2 during the reaction.

The O 1s spectra show three features (Figure 5), i.e., the peak for a lattice oxygen peak (designated as O_L at the most negative binding energy), followed by the peak for surface-adsorbed oxygen species (designated as O_{ads}).[41] The peak at the most positive binding energy most likely represents the presence of an amorphous carbonaceous species. The relative ratio of O_{ads} (%) versus total area in O 1s spectra reveals that the highest concentration of surface oxygen species follows the decreasing trend CZLPN > CZLNS > CZLPY > CZLSY > CZLPS > CZLNY. Relative ratios (%) of O_{ads}/total area, $Ce^{3+/4+}$ and $Pr^{3+/4+}$ calculated from the area under the deconvoluted curves are shown in Table S6.

Zr 3d spectra (Figures S11) show two different environments for Zr (most likely corresponding to surface hydroxyls at more negative binding energy of each orbital split and ZrO_2 at more positive binding energy).[22] Two different Y environments can also be confirmed based on the Y 3d spectra fitting (most likely originating from yttrium oxide at more negative binding energy for each orbital split and yttrium carbonates at more positive binding energy, Figure S12).[42]

Fitting Ce 3d spectra is challenging. The Ce 3d spectrum for oxidized CeO_2 has six peaks originating from three pairs of spin−orbit doublets. They are usually labeled with u, u″, and u‴ for $3d_{5/2}$ and v, v″, and v‴ for $3d_{7/2}$ spin−orbit components. On the other hand, Ce(III)-oxide shows two pairs of doublets labeled as v^0 and v′ for $3d_{5/2}$, and u^0 and u′ for $3d_{7/2}$.[43] CeO_2 reduction to Ce(III) will decrease the v‴ and u‴ peak intensities and increase the peak intensities for v′ and u′, which will result in the peak intensities decrease of u″ and v″. On the other hand, the
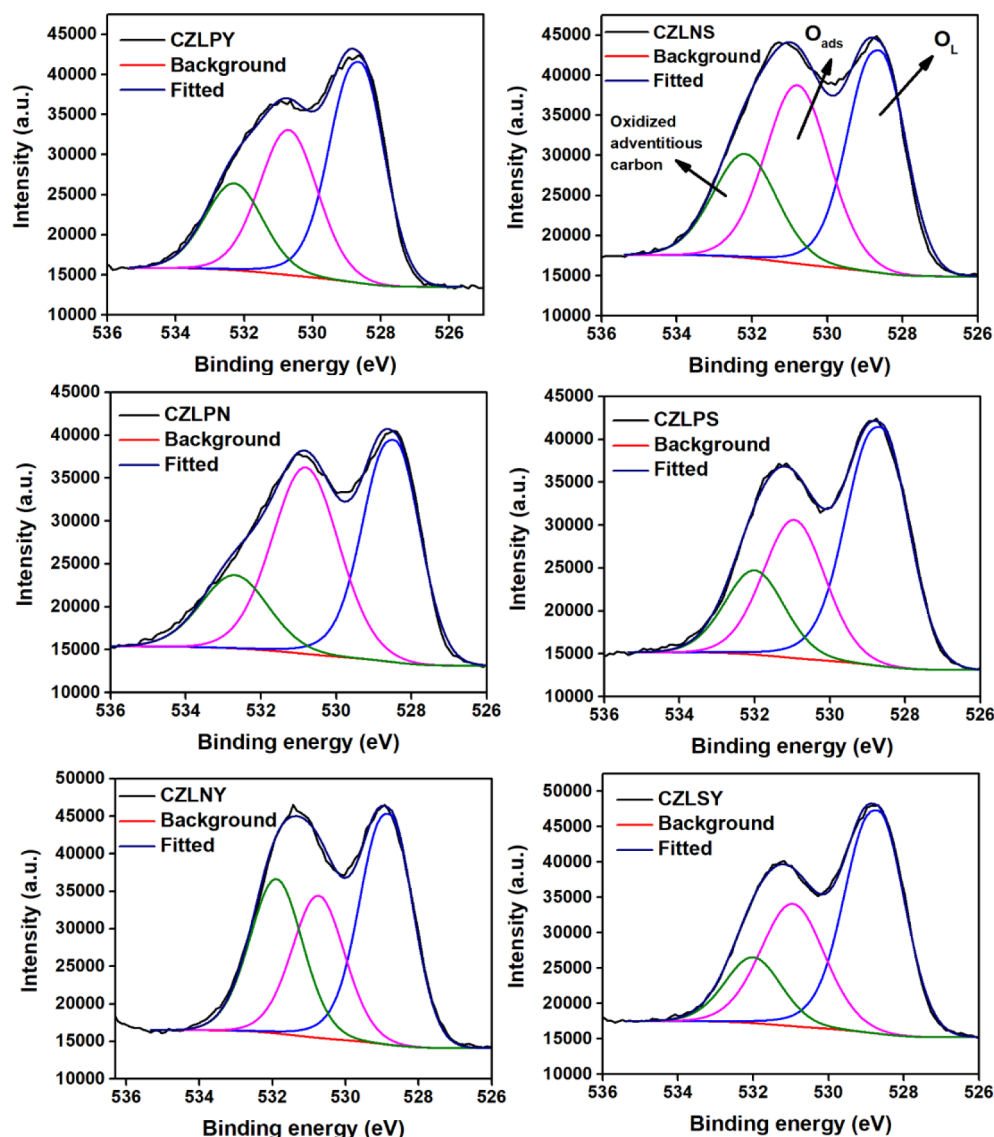
**Figure 5.** High resolution O 1s spectra of as-synthesized high-entropy compounds.

peaks for v^0 and u^0 are difficult to resolve due to a small peak energy difference compared to the peaks for v and u.[44] All fitted Ce 3d spectra are displayed in Figure S13. The calculated fraction of Ce^{3+} is in the following descending order: CZLNS (21.1%) > CZLSY > CZLNY > CZLPN ≈ CZLPS ≈ CZLPY, which corresponds well to the catalytic activity of high-entropy oxides as explained below.

The fitted Pr 3d spectra for the samples containing Pr are shown in Figure S14. The spectra were fitted following the detailed procedure presented previously[45] with three doublets labeled a/b, a′/b′, and a″/b″ and an additional feature Pr $3d_{3/2}$ labeled t. The shapes of the spectra and the fitted features are very similar for all three samples, suggesting that the Pr environment is similar. Doublet a″/b″ is not present for Pr_2O_3 and can, therefore, be assigned to Pr^{4+} ions.[45] However, at the high-binding energy side of the b″ peak, an intense oxygen Auger O_{KLL} peak is present, making fitting the b'″ peak difficult.

After conducting TGA/DSC analysis, XPS was employed to estimate the oxygen uptake process, indicating the incorporation of oxygen into the crystal lattice, subsequently leading to the oxidation of Ce^{3+} to Ce^{4+}. The results given in Figure S15 and Table S6 suggest oxygen uptake upon subjecting the best catalyst CZLNS to heating in an oxygen atmosphere at 600 °C. This observation agrees well with a decrease in the relative percentage of Ce^{3+} from 21.1% to 12.6%. Additionally, the spectrum of the O 1s exhibits an increase in the level of O_L and a decrease in the level of the levels of the O_{ads} species on the surface, confirming the incorporation of oxygen into the lattice structure.

3.6. Photocatalytic Performances. The results of HEO performance in photocatalytic CO_2 hydrogenation are presented in Figure S16. The photocatalytic activity of the HEO material was confirmed over 190 min of irradiation with the UV lamp, without co-catalyst addition. There are several factors that contribute to the elevated rate of CO production in current HEOs, including the existence of lattice defects like oxygen vacancies which serve as active sites,[46] the presence of five cations which increase activity through the synergistic effect,[47] a favorable electronic structure that supports the reactions of CO_2 conversion,[8] resulting from the defective nature of HEOs, to participate in photocatalytic reactions.
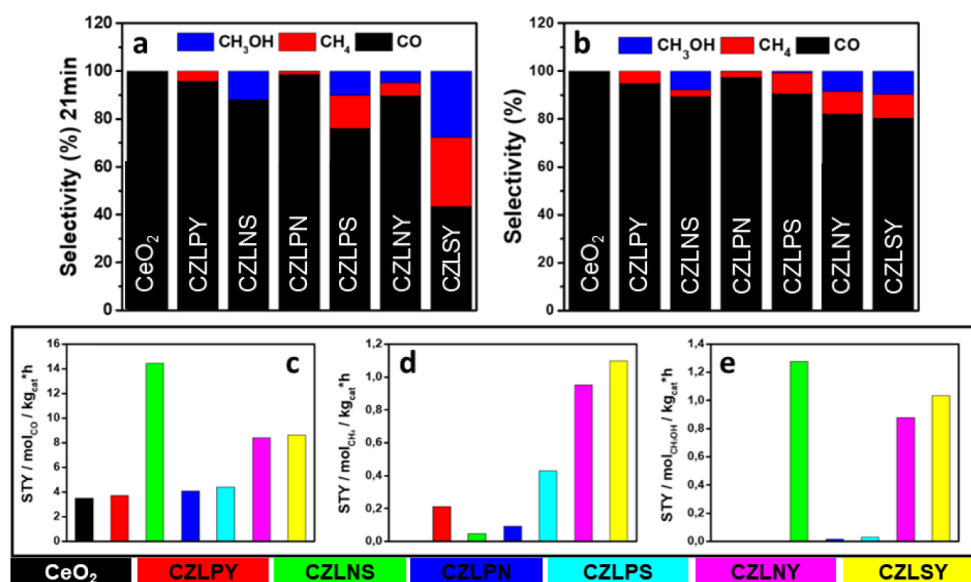
Figure 6. Selectivity of HEOs toward reaction products (a) after the first interval time (21 min) and (b) after the final interval time (189 min). Used HEO catalysts space-time yield toward reactions products (c–e).

In the study of photocatalytic CO_2 hydrogenation, six HEOs were tested with different combinations of Ce, Zr, La, Pr, Nd, Sm, and Y. The photocatalytic activity of each compound was evaluated, and the results showed that some compounds exhibited significantly better activity than the others. Overall results of the photocatalytic CO_2 hydrogenation are given in Table S7. The conversion of CO_2 to products was observed over a 10-time interval (21 min per interval, and 4 additional minutes for GC to get to ready state). As expected, pure CeO_2 showed the lowest conversion, with only 6.6%, while the CZLNS compound exhibited the highest conversion rate of 29.7%. The CZLPY compound showed a modest improvement with 7.4%, while the CZLPN and CZLPS compounds exhibited conversions of 7.9% and 9.2%, respectively. The CZLNY and CZLSY compounds showed a conversion of 19.3% and 20.3%, respectively. The significant improvement in the photocatalytic activity of CZLNS, CZLNY, and CZLSY compounds can be attributed to the presence of Nd and Sm, which are rare earth elements with mixed oxidation state (+2/+3). These elements possess unique optical and electronic properties that enhance the photocatalytic activity.[48,49] Additionally, the combination of Ce, Zr, and La with Nd and Sm played a crucial role in the enhanced activity. The CZLPY, CZLPN, and CZLPS compounds, on the other hand, showed only moderate improvements in photocatalytic activity compared to those of the pure oxide. One possible reason for the lack of improvement in these compounds could be the addition of Pr, but it did not significantly enhance the photocatalytic activity . Furthermore, the brown color of Pr-containing compounds may have hindered UV light absorption, leading to a lower activity.[50] Overall, the results indicate that the combination of Ce, Zr, La, Nd, Y, and Sm is more effective in enhancing the photocatalytic activity of HEOs for CO_2 hydrogenation. The selectivity of a photocatalytic reaction refers to the percentage of a specific product that is formed during the reaction, compared to the total amount of products, formed after final interval time and after first time interval is presented in Table S7 and Figure 6a,b.

The selectivity toward the products for all catalysts at the first-time interval (where the conversion is below 10% for most of the compounds), together with selectivity at the final time interval and the different time intervals, is presented in Figures 6a,b and S17, respectively. Pure ceria (CeO_2) was found to have 100% selectivity toward carbon monoxide (CO) in all reaction stages. However, the other compounds tested showed varying degrees of selectivity toward different products.

Among the tested compounds, CZLPY showed the highest selectivity toward methane (CH_4) in the first reaction time interval, but its selectivity shifted toward CO in the following reaction intervals. CZLPY showed a selectivity of 94.66% toward CO and 5.34% toward CH_4 at the final time interval. This suggests that the presence of Pr and Y in the composition may have favored the production of CO over CH_4. CZLNS showed a relatively high selectivity toward methanol (CH_3OH) in the first three-time intervals, but its selectivity shifted toward CO in the later stages of the reaction. CZLNS had a selectivity of 89.26% toward CO, 2.9% toward CH_4, and 7.84% toward CH_3OH at the final time interval. The presence of Nd and Sm in the composition may have contributed to the higher selectivity toward CH_3OH over CH_4. CZLPN and CZLNY showed consistently high selectivity toward CO in all reaction stages, with only minor amounts of CH_4 and CH_3OH being produced for CZLPN. At the final time interval, CZLPN showed a selectivity of 97.4% toward CO, 2.2% toward CH_4, and 0.4% toward CH_3OH. The presence of Pr and Nd in the composition may have contributed to the high selectivity toward CO. CZLPS had a relatively high selectivity toward CH_3OH in the first reaction point, but its selectivity shifted toward CO in the later stages. CZLPS showed a selectivity of 90.6% toward CO, 8.7% toward CH_4, and 0.7% toward CH_3OH at the final time interval. The presence of Pr and Sm in the composition may have contributed to the higher selectivity toward CH_4 over CH_3OH. CZLNY had a selectivity at the final time interval of 82.1% toward CO, 9.3% toward CH_4, and 8.6% toward CH_3OH. The presence of Nd and Y in the composition may have favored the production of CH_3OH over CH_4. Finally, CZLSY showed the lowest initial selectivity toward CO among all tested compounds, but its selectivity shifted toward CO as the reaction progressed. At the final point, CZLSY showed a selectivity of

80.2% toward CO, 10.2% toward CH_4, and 9.6% toward CH_3OH. The presence of Sm and Y in the composition may have contributed to the similar selectivity toward CH_4 and CH_3OH.

First, it is evident that the pure ceria compound (CeO_2) has a 100% selectivity toward CO in all reaction stages, which is consistent with its known activity as an efficient oxygen storage material.[51,52] Regarding the high-entropy compounds, it can be seen that most of them show a high selectivity toward CO at the final time interval, ranging from 82.1% to 97.4%. This indicates that the presence of ceria and zirconia in the catalysts is essential for the CO_2 hydrogenation reaction,[53] as these elements are known to have a high affinity for CO_2 and can facilitate the adsorption of CO_2 onto the catalyst surface.[54,55] In terms of the selectivity toward CH_4 and CH_3OH, some correlations can be made. For instance, high-entropy oxides that contain La, Pr, Nd, and Sm tend to show a higher selectivity toward CH_4, while those containing Y tend to show a higher selectivity toward CH_3OH (CZLNY and CZLSY). This suggests that the selectivity toward these products may be related to the presence of these specific elements in the catalysts. Moreover, it is interesting to note that the selectivity toward CH_4 tends to decrease over time in most of the compounds, while the selectivity toward CO tends to increase. This could be explained by the fact that the CO_2 hydrogenation reaction involves a series of steps, where CO_2 is first adsorbed onto the catalyst surface and then reduced to CO,[56,57] which can subsequently undergo further reduction to produce CH_4. Thus, the selectivity toward CH_4 could be affected by the availability of CO on the catalyst surface, which may decrease over time as more CO_2 is adsorbed.

Figure 7 illustrates the comparison of total CO_2 conversion using pure CeO_2 and HEOs as catalysts. The results show that
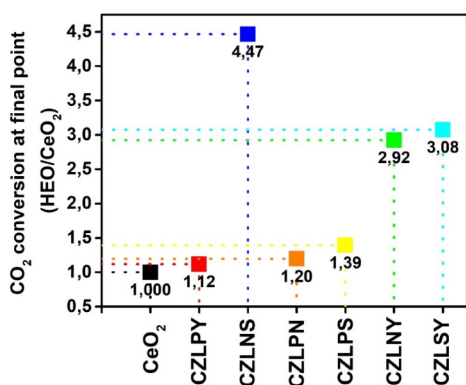

Figure 7. Comparison of CO_2 conversion over HEOs vs CeO_2 conversion at the final point.

the photocatalytic activity of the HEO compounds is significantly higher than that of CeO_2. In particular, CZLNS improves the photocatalytic activity by 4.47 times, while CZLPY shows only a modest improvement of 1.12 times compared to pure CeO_2.

Table 2 presents the overall comparative results of the structural and spectroscopic characterization, physisorption measurements (BET surface area), and conversion of CO_2 for the high-entropy oxide compounds. The results indicate that the CZLNS compound has one of the highest surface area and pore volume, along with CZLNY and CZLSY. The bandgap values of the compounds range from 2.65 to 3.37 eV, with CZLNY having the highest value and CZLPN the lowest. In terms of photocatalytic activity, the results show that CZLNS has the highest CO_2 conversion efficiency, which is 4.47 times higher than that of pure CeO_2. CZLPY has a moderate photocatalytic activity with a 1.12 times improvement compared to pure CeO_2, while CZLNY and CZLSY have slightly lower photocatalytic activity than CZLNS. The three compounds with the highest conversion efficiency CZLNS, CZLSY, and CZLNY are Pr-free compounds implying that their bandgaps are among studied catalysts larger (>3 eV) due to the fact that Pr 4f states lower bandgap values of parent pristine CeO_2 compound. It also follows that these catalysts absorb light only in the UV part of the spectrum as evidenced from absorption spectra. From Table 2, it is also evident that these catalysts have the largest BET surface area, the highest Ce^{3+}/Ce^{4+} ratio, quite a high lattice microstrain and a pretty high concentration of surface oxygen species including oxygen vacancies. All of these findings measure the availability of catalytically active sites required for successful and efficient catalytic conversion of CO_2. The key structural parameter that mostly affects the catalytic activity of studied HEOs is the fraction of Ce^{3+} species as nicely presented in Table 2.

An additional point of the research was to investigate the photocatalytic activity of HEOs when the entropy is introduced step by step, in a way previously reported.[58,59] The research started by comparing the activity of CeO_2, which served as a baseline. Since all the high-entropy compounds contained Ce, Zr, and La, and among all, CZLNS catalysts exhibit the highest CO_2 conversion, the next compounds to be tested were the oxides containing four elements in equimolar ratio, namely, Ce, Zr, La, and Nd/Sm, the so-called medium-entropy oxides. The goal was to observe the trends in selectivity toward reaction products and CO_2 conversion in general and to establish a connection between the activity of each element and its influence on the catalytic activity. The overall results of the catalytic activity of medium-entropy oxides are shown in Table S8 and Figure 8. In addition to exploring the effect of entropy

Table 2. Overall Results of Using Ceria-Based HEOs for Photocatalytic CO_2 Hydrogenation. The Bold Text Denotes the Catalysts with the Highest Activity Expressed with the Conversion Rate

compound	average crystallite size (nm)	lattice microstrain ($\times 10^{-4}$)	S_{BET} (m^2g^{-1})	Ce^{3+} ratio $[Ce^{3+}]/[Ce^{3+}+ Ce^{4+}]$[rel.%]	oxygen species concentration $[O_{ads}]/[$Total area$]$[rel.%]	bandgap (eV)	conversion (%)
CeO_2	11	20.56	21.5	n/a	n/a	3.74	6.6
CZLPY	4	67.11	24.9	7.5	33.1	2.73	7.4
CZLNS	**4**	**93.38**	**33.2**	**21.1**	**37**	**3.32**	**29.7**
CZLPN	4	79.53	27.3	6.1	41.6	2.65	7.9
CZLPS	5	59.02	24.2	7.4	30.1	2.93	9.2
CZLNY	**4**	**72.68**	**35.7**	**18.3**	**26.9**	**3.37**	**19.3**
CZLSY	**4**	**74.35**	**32**	**20.6**	**31.5**	**3.21**	**20.3**
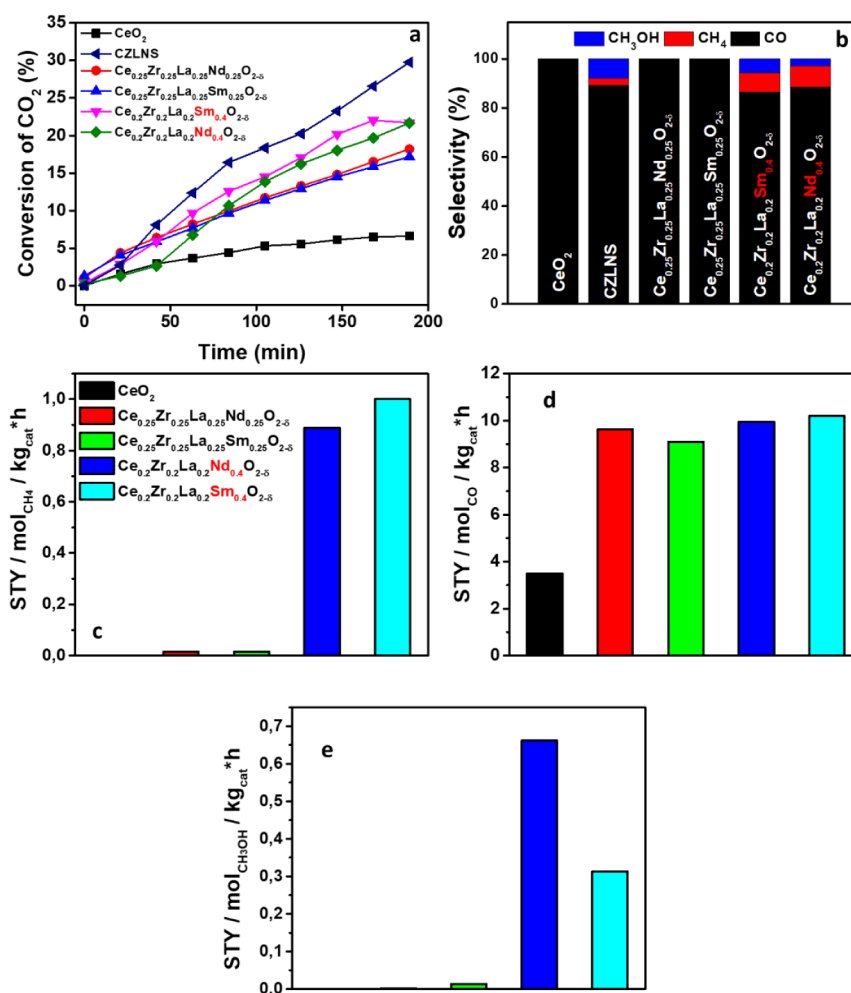
Figure 8. Photocatalytic CO_2 conversion using medium-entropy oxide catalysts compared with CZLNS and CeO_2 as baseline (a); selectivity of the medium-entropy oxide catalysts toward reaction products at the final time interval (189 min) of the reaction (b), used medium-entropy catalysts space-time yield toward reactions products (c−e).

introduction, we also investigated the impact of increasing the concentration of Nd and Sm in the medium-entropy oxides. To do so, the same amount of Ce, Zr, and La was used as in the high-entropy form (0.2), but increased the concentration of Nd and Sm to 0.4. Catalytic activity of medium-entropy oxide systems resulted in interesting outcomes in terms of their photocatalytic activity and selectivity for CO_2 hydrogenation. The $Ce_{0.25}Zr_{0.25}La_{0.25}Nd_{0.25}O_{2-\delta}$ exhibited a CO_2 conversion rate of 18.2%, with an almost 100% selectivity toward CO. Similarly, the $Ce_{0.25}Zr_{0.25}La_{0.25}Sm_{0.25}O_{2-\delta}$ oxide showed a CO_2 conversion rate of 17.2% with selectivity almost exclusively toward CO. On the other hand, increasing the concentration of Nd or Sm in the Ce−Zr−La−Nd and Ce−Zr−La−Sm medium−entropy oxides, while keeping the concentration of Ce, Zr, and La constant at 0.2, resulted in higher CO_2 conversion rates. The $Ce_{0.2}Zr_{0.2}La_{0.2}Nd_{0.4}O_{2-\delta}$ oxide system exhibited a CO_2 conversion rate of 21.7%, with a selectivity of 88.59% toward CO, 8.69% toward CH_4, and 2.72% toward CH_3OH. Meanwhile, the $Ce_{0.2}Zr_{0.2}La_{0.2}Sm_{0.4}O_{2-\delta}$ oxide system also showed a CO_2 conversion rate of 21.7%, but with a selectivity of 86.53% toward CO, 7.72% toward CH_4 and 5.75% toward CH_3OH, as shown in Figure 8.

The results of this research showed that the catalytic properties of HEOs can be tuned by selecting the appropriate

constituents. Specifically, we found that ceria-based HEOs have great potential as photocatalysts for CO_2 hydrogenation reaction, when tuned correctly.

The overall catalytic activity of the various compounds was evaluated by calculating the spatial time yield (STY). STY values were calculated by using eq 3. Total inlet volumetric feed flow rate (Q_{in}): 15 mL/min. Proportion of CO_2 in the inlet feed was fixed to 0.33 (V_{in}), V_g represents molar volume of ideal gas at STP, while remaining parameters used were catalysts weight (m_{cat}), conversion of CO_2 (X_{CO_2}), and selectivity toward reaction product (S_i).

$$STY_i \left[\frac{mol}{kg_{cat}\, h} \right] = \frac{Q_{in} V_{in} \left(\frac{X_{CO_2}}{100} \right) \left(\frac{S_i}{100} \right)}{V_g m_{cat}} \tag{3}$$

The compounds tested include pure ceria, medium-entropy oxides, and six HEOs. Among the HEOs, the CZLNS compound showed the best activity, with an STY of 14.4 $mol_{CO}\, kg_{cat}^{-1}\, h^{-1}$. In terms of activity toward the production of CH_4, the CZLSY compound showed the best activity with an STY of 1.09 $mol_{CH4}\, kg_{cat}^{-1}\, h^{-1}$. Regarding the activity toward CH_3OH production, the CZLNS compound exhibited the best performance with an STY of 1.27 $mol_{CH_3OH}\, kg_{cat}^{-1}\, h^{-1}$. These results additionally suggest that HEOs can be considered as
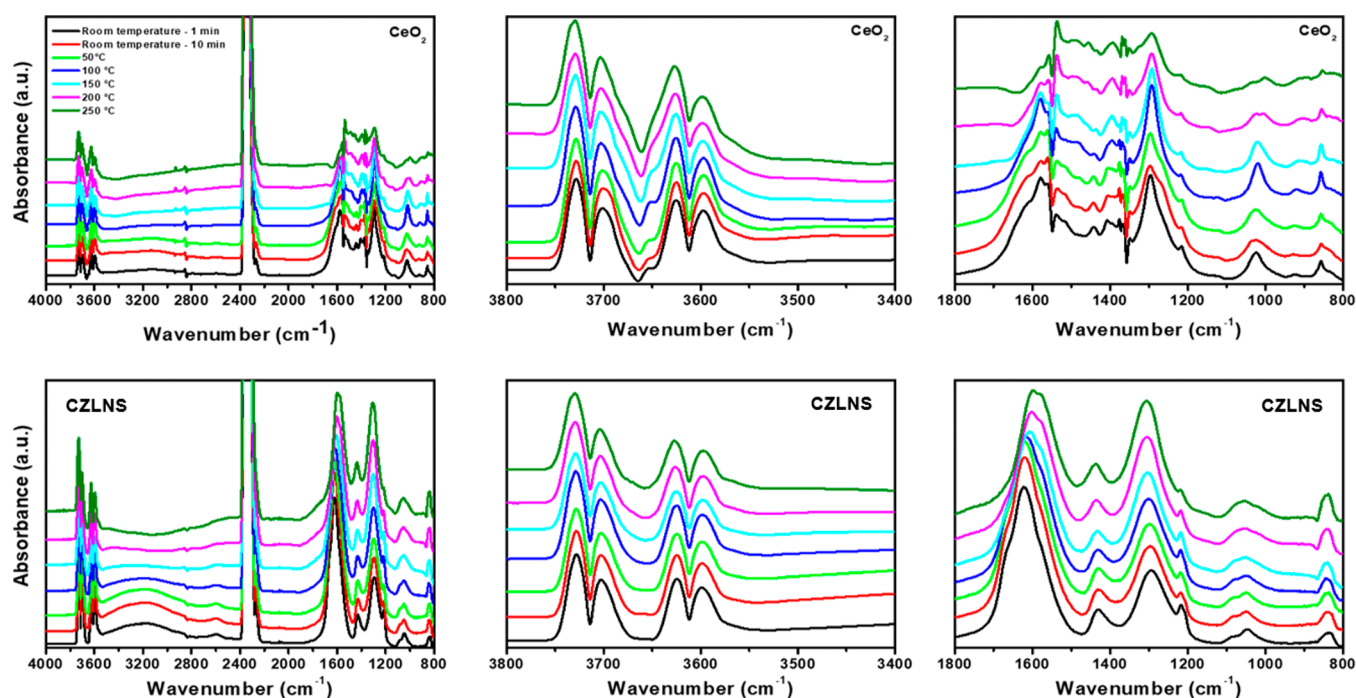
Figure 9. In situ IR spectra for CeO_2 (top) and the best CZLNS compound (bottom), under the reaction conditions.

promising catalysts for CO, CH_4, and CH_3OH production in CO_2 hydrogenation reactions. The results are shown in Figures 6c−e, 8c−e and Table S9.

Comparing the results of photocatalytic activity, specifically regarding STY values, across different studies presents a challenge due to the diverse experimental setups and conditions employed. Discrepancies in gas composition, sources of radiation, reaction parameters, different reactors, and catalyst properties significantly influence the observed photocatalytic performance. Nonetheless, despite these challenges, it remains essential to provide an overview of the field's progress. In this work, CeO_2 exhibited CO production rate of 3.5 mmol $g^{-1} h^{-1}$, while the best catalyst (CZLNS) exhibited 14.4 mmol $g^{-1} h^{-1}$. In previously published papers, there are many reported photocatalysts used in photocatalytic CO_2 reduction reaction. For instance, Shangguan et al.[60] used quantum-sized Au nanoparticles with a diameter of aproximately 4 nm as the photocatalyst and exhibited CO evolution up to 4.73 mmol $g^{-1}h^{-1}$ (accompanied by O_2 evolution) at 200 °C while using different LED light sources (365−620 nm) and different light intensities. Zhao et al.[61] used FeO-CeO_2 nanocomposites as the photocatalyst under Xe lamp irradiation and heating up to 419 °C, which resulted with a CO production rate of 19.61 mmol g^{-1} h^{-1}. Pu et al. also investigated photocatalytic CO_2 reduction over a CeO_2/g-C_3N_4 catalyst under different atmospheres.[62] The catalyst under an N_2 atmosphere showed the best photocatalytic activity with a production rate of 3.5 μmol $g^{-1}h^{-1}$ under full spectrum illumination (300 W Xe lamp) and the presence of water vapor through 8 h. Just for comparison, commercially available photocatalyst TiO_2 P25 was tested by Akrami et al.[13] alongside synthesized $TiZrNbHfTaO_{11}$ high-entropy oxide, using 400 W Hg lamp, with reported 4.63 μmol $g^{-1}h^{-1}$, and 4.64 μmol $g^{-1}h^{-1}$ CO production rates, respectively.

3.7. Diffuse Reflectance Infrared Spectroscopy (DRIFTS). DRIFTS analysis was employed to investigate the mechanism behind the CO_2 hydrogenation process in both parent and modified HEO (CZLNS) compounds as depicted in
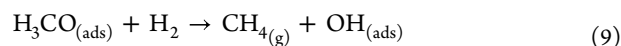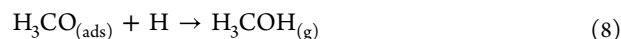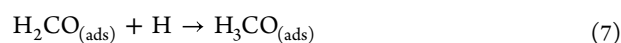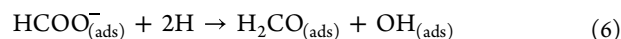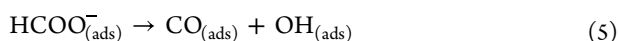
Figure 9. CZLNS compound exhibited stronger signal intensities, indicating more effective CO_2 adsorption, consistent with catalytic performance. Similarities between spectra of CeO_2 and CZLNS can be noticed, which is consistent to material characterization results, which again confirms that the ceria-based HEOs are indeed modified versions of CeO_2. A distinct IR band at 2350 cm^{-1} indicated the presence of gaseous CO_2. Overtones of gas-phase CO_2 and OH bonds were observed between 3590 and 3730 cm^{-1} in both CeO_2 and CZLNS compounds.[63] A broad band in the 1600−800 cm^{-1} range corresponds to intense C−O vibration modes associated with surface carbonates, carboxylates, formates, and alkoxides. Vibrations related to C−H bonds were detected between 2800 and 3000 cm^{-1}, with a minor peak at 2858 cm^{-1} attributed to C−H vibrations of surface formate species,[63] although gas phase CH_4 was not visible as it typically emerges at higher reaction temperatures (>250 °C). The process of CO_2 hydrogenation involves hydrogen dissociation, OH formation, and CO_2 activation.[63,64] This results with the formation of $CO_2^{\delta-}$ species (activated), which then interact with OH groups to form bicarbonates.[64] IR bands at 1600−1300, and around 1220−1210 cm^{-1} represent various vibrational modes of bidentate bicarbonates.[65] When temperatures rise, surface monodentate and bidentate carbonates and carboxylates become visible through IR bands, each exhibiting intensities and stabilities across the catalysts.[66,67] The formation of formate plays a crucial role as an intermediate in the CO_2 hydrogenation process. Formate can exist as either monodentate or bidentate and originates from carboxylates or bicarbonates (eq 4).[67−69] Characteristic vibrations of formate, including bidentate and monodentate forms, are detected in the 2800−2900 cm^{-1} range for ν(CH) and in the 1600−1300 cm^{-1} range for asymmetric and symmetric modes of $\nu(CO_2)$. Deformation modes $\delta(CO_2)$ are detectable below 1000 cm^{-1}. Formate on catalysts can either desorb as CO or react further with hydrogen to produce methane (eq 5).[63] Among the catalysts studied, CO formation is preferred, while adsorbed CO has a lifespan on oxide surfaces—
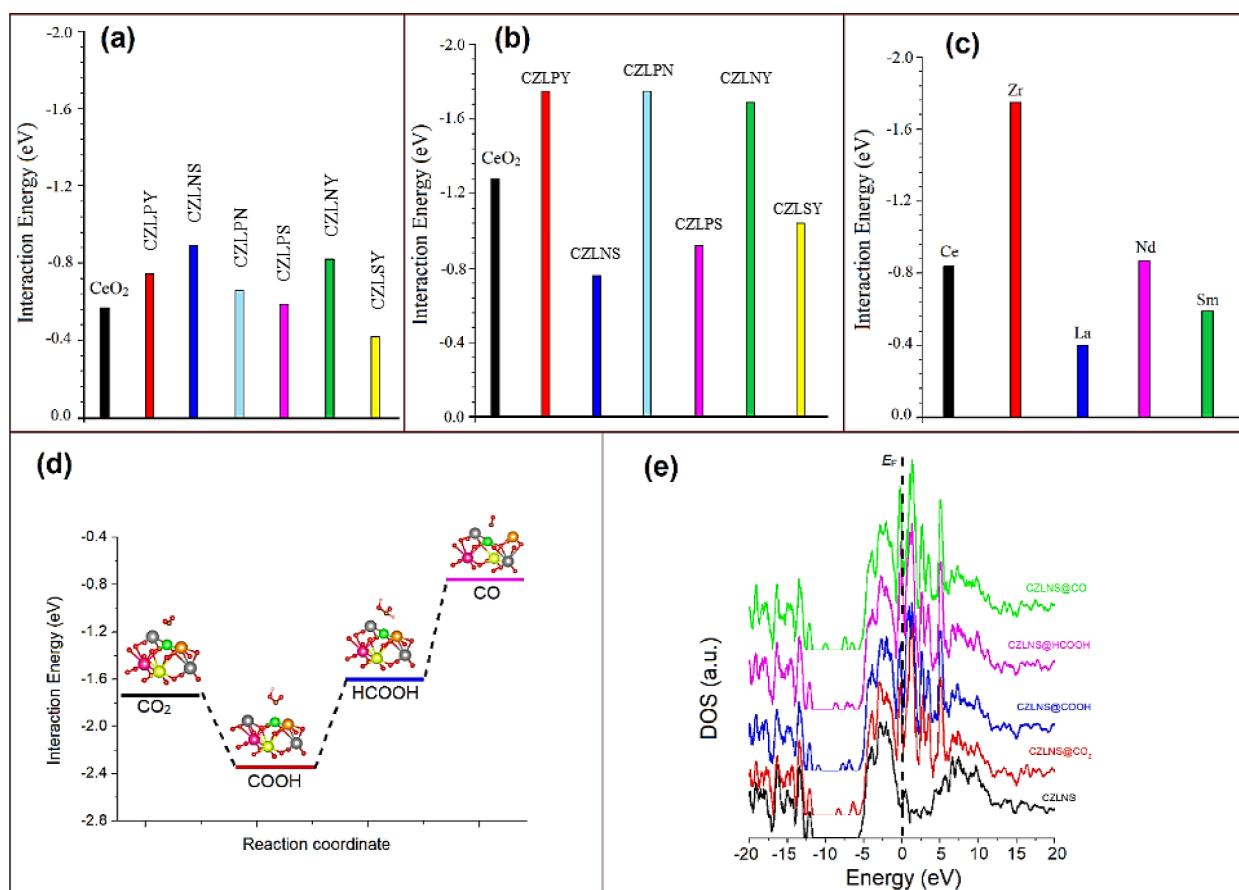
Figure 10. Interaction energy of five CO_2 molecules (a) and five CO interaction energies (b) over the surfaces of investigated HEOs along with ceria. The one with the highest CO_2 adsorption (interaction) energy means high CO_2 reduction ability. CO interaction energy over the surfaces of investigated HEOs; to find the best species that can desorb CO. The one with the lower interaction energy means high desorption. Single CO_2 molecule interaction energy over the surface CZLNS (best HEO); at five different positions (Ce, Zr, La, Nd, and Sm) to find the most active site (c). Energy level diagram of CO_2RR intermediates (d) and comparative DOS plot of pristine CZLNS and $-CO_2$, $-COOH$, $-HCOOH$, and $-CO$ adsorbed CZLNS. The Fermi energy is set to zero and shown as black dotted lines (e).

either desorbing or partially reacting with hydrogen to produce oxygenated hydrocarbon fragments such as HCO, HCOH, H_2CO, and H_3CO. IR bands around $1050-1000$ cm^{-1} indicate the C−O stretching modes which are partially attributed to alkoxide species.[70] Vibrations around $1450-1400$ cm^{-1} for CeO_2 and 1420 cm^{-1} for CZLNS are associated with alkyl groups, which may overlap with carbonate and formate species, after methanol dissociatively adsorbs on a surface of the catalysts.[71]

The main mechanism in the process of CO_2 hydrogenation involves the decomposition of HCOO intermediates to form CO. During the catalytic process, three primary products are generated: CO, along with small amounts of CH_4 and CH_3OH over the CZLNS catalyst. This could be explained by an alternative reaction pathway that results in the production of alcohols from formate. Initially, from a kinetic perspective, formaldehyde formation is more favorable, which is then converted into methoxy species.[63] Microkinetic analysis has confirmed that the HCOO$^-$ route is the predominant pathway for methanol formation on ceria-based catalysts, which subsequently undergoes hydrogenation to form methane (eqs 6−9).[63,64]

$$HCO_{3(ads)}^- + H_{(ads)} \rightarrow HCOO_{(ads)}^- + OH_{(ads)} \tag{4}$$

$$HCOO_{(ads)}^- \rightarrow CO_{(ads)} + OH_{(ads)} \tag{5}$$

$$HCOO_{(ads)}^- + 2H \rightarrow H_2CO_{(ads)} + OH_{(ads)} \tag{6}$$

$$H_2CO_{(ads)} + H \rightarrow H_3CO_{(ads)} \tag{7}$$

$$H_3CO_{(ads)} + H \rightarrow H_3COH_{(g)} \tag{8}$$

$$H_3CO_{(ads)} + H_2 \rightarrow CH_{4(g)} + OH_{(ads)} \tag{9}$$

3.8. Characterization of the Material After Photocatalytic Reaction.
In order to evaluate the material (CZLNS) after the catalytic reaction of photocatalytic CO_2 hydrogenation, several analyses were conducted. These included X-ray diffraction (XRD) to assess the crystallographic data, scanning electron microscopy (SEM) to examine any possible morphology changes, and X-ray photoelectron spectroscopy (XPS) to analyze the surface composition. The XRD analysis (Table S10) revealed a slight increase in the average crystallite size of the material and a significant decrease of coupled lattice microstrain, which can be attributed to the pretreatment at a higher temperature. Additionally, there was a slight decrease observed in the lattice parameters and cell volume. This decrease could potentially be explained by an increase in the concentration of Ce^{3+} ions resulting from the hydrogenation reaction. SEM images (Figure S18) showed that the surface morphology of the material remained unchanged after the catalytic reaction. This indicates that the reaction did not cause any significant

alterations in the surface structure. Elemental mapping also demonstrated that the distribution of elements remained uniform, further confirming the stability of the material's composition (Figure S19). The deconvolution analysis of the Ce 3d spectrum for CZLNS after the reaction revealed an increase in the concentration of Ce^{3+} ions compared to its as-synthesized form, which is consistent with crystallographic data obtained from the Rietveld refinement. This suggests that the hydrogenation reaction led to the reduction of surface Ce^{4+} species to Ce^{3+} ions. Furthermore, the deconvolution analysis of the O 1s spectrum for CZLNS after the reaction showed a decrease in the concentration of adsorbed oxygen species compared to the as-synthesized CZLNS. This decrease indicates that these oxygen species likely participated directly in the CO_2 hydrogenation reaction. Additionally, deconvoluted XPS spectra are shown in Figure S20.

3.9. First-Principles Density Functional Theory Simulations of HEOs. As outlined in our previous research, similar methodologies have been employed for doping, resulting in the construction of six distinct HEOs models.[22] These include $Ce_{0.2}Zr_{0.2}La_{0.2}Pr_{0.2}Y_{0.2}O_2$ (CZLPY), $Ce_{0.2}Zr_{0.2}La_{0.2}Nd_{0.2}Sm_{0.2}O_2$ (CZLNS), $Ce_{0.2}Zr_{0.2}La_{0.2}Pr_{0.2}Nd_{0.2}O_2$ (CZLPN), $Ce_{0.2}Zr_{0.2}La_{0.2}Pr_{0.2}Sm_{0.2}O_2$ (CZLPS), $Ce_{0.2}Zr_{0.2}La_{0.2}Nd_{0.2}Y_{0.2}O_2$ (CZLNY), and $Ce_{0.2}Zr_{0.2}La_{0.2}Sm_{0.2}Y_{0.2}O_2$ (CZLSY), as depicted in Figure S21. It should be noted at this point that the oxygen site in HEO lattices was considered as fully occupied in the theoretical modeling. The DFT-optimized bulk structures were cleaved in various directions, revealing that the surface along the (001) direction exhibits high stability. To identify the most effective catalyst, all of these slabs, along with pristine ceria, were optimized as illustrated in Figure S22. Subsequently, five CO_2 molecules were adsorbed at five distinct positions on the slab of these HEOs due to the presence of five different types of atoms, as shown in Figure S23. The interactions between CO_2 molecules and catalyst surfaces were simulated using the following equation:

$$\Delta E_{ad} = E_{surface@analyte} - (E_{analyte} + E_{surface}) \qquad (10)$$

In this equation, $E_{surface@analyte}$ represents the adsorption energy of the intermediate species, $E_{analyte}$ corresponds to the DFT energies of the relaxed slabs with the specific adsorbate, $E_{surface}$ signifies the DFT energy of the slab without any adsorbate, and $E_{analyte}$ stands for the DFT energies of the molecular gas-phase references.

Based on the CO_2 interaction energy (-0.89 eV), it is determined that CZLNS is the superior catalyst for CO_2 reduction compared to the other HEOs. The 2D electron localization function (ELF) plots of all seven species, as shown in Figure S24, indicate that the CO_2 molecules excellently share electronic cloud density with the catalyst surfaces. A comparative analysis of Figure S24 suggests that all HEOs are active and capable of reducing the level of CO_2. The interaction energy of CO_2 with all of these species is depicted in Figure 10a, a finding that aligns with our experimental data.

Similarly, to identify and verify whether the same catalyst can desorb the CO molecules, we interacted with five CO molecules on the surface of all these HEOs and simulated their interaction energy. The optimized models and ELF maps are presented in Figures S25 and S26, while the interaction energy can be seen in Figure 10b. A comparative analysis of Figures S25, S26, and Figure 10b leads to the conclusion that CZLNS is again the best catalyst for CO desorption, exhibiting a minimum interaction energy (-0.76 eV). This lower interaction energy indicates that

CO molecules will not adhere to the surface of CZLNS and only a small energy barrier is required for CO desorption.

After confirming CZLNS as the best catalyst, we investigated its most active site (most reactive atoms). To perform this study, we individually interacted one CO_2 molecule with each of the Ce, Zr, Nd, La, and Sm atoms on the catalyst and simultaneously simulated their interaction energies, as depicted in Figure 10c. From the comparative interaction energy analysis, it is inferred that Zr is the most reactive site for CO_2 reduction, exhibiting the highest adsorption energy.

To streamline the discussion, we focused our simulation on the CZLNS model and conducted all of the electronic structure properties and CO_2 reduction studies. This model displayed ideal interaction energy with CO_2 and CO molecules. The conversion of the CO_2RR into CO occurs via three intermediate steps:

Formation of COOH: In the first step, CO_2 is converted into the intermediate COOH (carboxyl group) with the addition of electrons and protons: $2 CO_2 + 2 e- + 2 H+ \rightarrow 2 COOH$.

Formation of HCOOH: The COOH intermediate further transforms into formic acid (HCOOH) with the addition of electrons and protons: $2COOH + 2 e- + 2 H+ \rightarrow 2 HCOOH$.

Formation of CO: The final step reduces formic acid (HCOOH) or carboxyl groups (COOH) to produce carbon monoxide (CO): $2 HCOOH + 2 e- + 2 H+ \rightarrow 2 CO + 2 H_2O$.

We optimized the adsorption configurations of reactants, intermediates, and products on the (001) facet of CZLNS as shown in Figure S27. The adsorption energies of CO_2 intermediate species were calculated using eq 4. The CO_2RR begins with the adsorption of CO_2 on the catalyst surfaces. Here, the adsorption energy of CO_2 on the surface of CZLNS is -1.74 eV. This high energy demonstrates excellent conversion of the CO_2RR over the surface of CZLNS.

As discussed earlier, the CZLNS surface catalyzes the CO_2 reduction reaction via a sequence of intermediates: $CO_2^* \rightarrow COOH^* \rightarrow HCOOH^* \rightarrow CO^*$. The adsorption energy of each intermediate (E_{ads}) determines its stability and reactivity on the surface as shown in Figure 10d and Table S11. A more negative E_{ads} implies a stronger intermediate-surface interaction and higher stability but also a lower tendency to desorb or react further. Thus, each intermediate faces a trade-off between stability and reactivity. A moderate E_{ads} is desirable to enable both the adsorption and desorption of intermediates. In our case, COOH* exhibits the most negative E_{ads} (-2.34 eV), indicating that it is the most stable and least reactive intermediate on the CZLNS surface. This high E_{ads} results from the strong bonding and anionic state of COOH*. Conversely, the adsorption energy of CO* is -0.76 eV, suggesting that it is a stable intermediate on the CZLNS surface. Therefore, the CZLNS surface favors the CO_2 reduction reaction and may promote desorption of CO, enhancing its selectivity. As the final product, weak adsorption is expected for CO. However, too negative E_{ads} should be avoided as it may impede the release of CO. The binding strength of these four intermediates could also be inferred from comparing the density of states (DOS) of the active Zr site with adsorbates (Figure 10e). As can be seen from Figure 10e, all of these intermediate species have additional peaks near the Fermi level compared to pristine CZNLS, corresponding to the stronger adsorbate binding energies.

As a result, the reduction of CO_2 to CO was found to be most energetically favorable. Additionally, HCOOH* has an intermediate E_{ads}, implying that it has moderate stability and
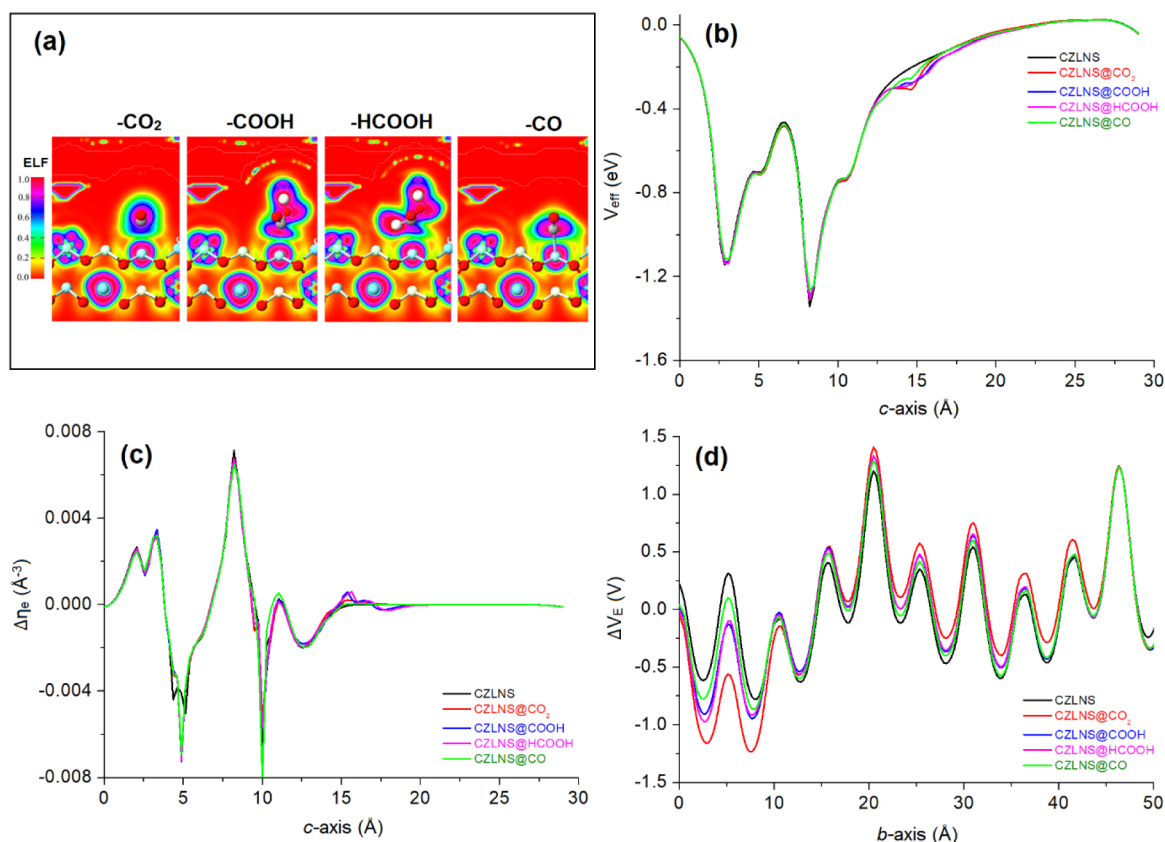
Figure 11. a) Comparative density of states and b) 2D effective potential map along c-axis. c) Electron difference density along c-axis and d) electrostatic difference density along b-axis of pristine CZLNS and CO_2 interacted intermediates.

reactivity on the CZLNS surface. This may be beneficial for the CO_2 reduction reaction as it may balance between stability and reactivity and facilitate both formation and desorption of HCOOH*. CO_2* has a reasonable E_{ads}, meaning that it is adsorbed on the CZLNS surface. This is advantageous for initiating the activation of CO_2 and increasing the reaction rate.

Based on our DFT simulations, we conclude that CZLNS demonstrates both high selectivity for CO and significant activity in CO_2 reduction. Our analysis suggests that the rate-limiting step in this process may involve the formation of COOH*, while the most favorable product appears to be CO*. To summarize, our findings strongly indicate that the CZLNS surface serves as an efficient catalyst for the CO_2 reduction reaction. The robust binding of COOH* and HCOOH*, combined with the moderate adsorption of CO_2* and CO*, supports the notion that this surface can facilitate the various stages of the reaction. These adsorption energy profiles signify a promising potential for catalytic activity in the conversion of CO_2 into CO when HEO materials enriched with elements such as La, Ce, Zr, Sm, and Nd.

In Figures 11a and S28, the sharing of electron cloud density between the CO_2RR intermediates and the surface of pristine CZLNS is clearly visible from the electron localization function (ELF) maps. The strong interaction between the CO_2 intermediates and the CZLNS surface can also be observed from the 2D effective potential map near 15 Å (Figure 11b), where pristine CZLNS is compared with the CO_2RR intermediates. Additionally, from CO_2RR intermediates, we calculated the electron difference densities (EDDs) and electrostatic difference potential (EDP) of pristine CZLNS

with and without CO_2 intermediates interactions, as shown in Figure 11c,d, respectively. The ELF, EDD, and EDP of the pure CZLNS catalyst and CO_2RR intermediates attached to CZLNS clearly demonstrate the electron transfer from the surface atoms to the CO_2RR intermediates.

Particularly, CZLNS@CO_2 is more prominent compared to other species, as can be seen from the EDP in Figure 11d. A comparative analysis of Figure 11 leads us to predict that, at the Zr sites of the CZLNS catalyst, we noted the buildup of charges, which facilitated the subsequent electron transfer from the catalyst to the CO_2 molecule. Remarkably, the electron transfer phenomenon is exclusively confined to the Zr sites, playing a crucial role in activating CO_2 and instigating the reduction process.

4. CONCLUSIONS

To summarize, we have successfully synthesized six types of phase pure ceria-based high-entropy oxides in nanocrystalline form using a modified aqueous sol−gel route. Thorough structural and surface analysis using various characterization methods (PXRD, SEM, TEM, BET, UV−Vis, XPS, and DRIFTS) has revealed that the obtained HEOs have a single fluorite structure with a lattice parameter similar to that of parent simple oxide CeO_2. The variation of equimolar chemical composition yielded the bandgap variation and modulation of electronic structure. The phase stabilization of HEO in parent CeO_2 lattice induced more lattice distortion, more Ce^{3+} concentration, more oxygen vacancies, and additional energy levels as compared to pristine CeO_2. Based on the obtained results, the compound $Ce_{0.2}Zr_{0.2}La_{0.2}Nd_{0.2}Sm_{0.2}O_{2-\delta}$ (CZLNS)

exhibited the best catalytic activity and space-time yield among all tested catalysts. This is attributed primarily to its unique chemical composition and comparative properties among studied catalysts: the highest lattice microstrain, the highest fraction of surface oxygen species including oxygen vacancies, high fraction of Ce^{3+}, high BET surface area, and the absence of Pr cations. Additionally, through DRIFTS analysis, we gained insights into the mechanism behind CO_2 hydrogenation over both CeO_2 and the best high-entropy oxide. In these processes, carbon monoxide (CO) was found to be the product with 100% selectivity when pure CeO_2 was used as a catalyst. On the other hand, "modified ceria"−HEOs displayed a preference for producing other reaction products such as methane and methanol. Importantly, these experimental observations align with theoretical models, including density functional theory (DFT) simulations. Finally, DFT simulations highlight CZLNS as an efficient catalyst for CO_2 reduction, demonstrating high selectivity for CO and significant activity, with COOH* formation potentially serving as the rate-limiting step and CO* as the favored product. This work delivered a promising way for designing new catalysts by combining high-entropy stabilization, nanoengineeringand theoretical modeling, bringing more opportunities for their applications in CO_2 conversion under UV light irradiation.

■ ASSOCIATED CONTENT

Ⓢ Supporting Information

The Supporting Information is available free of charge at https://pubs.acs.org/doi/10.1021/acsami.4c00478.

> Supplementary data including XRD patterns (Figure S1), crystallographic data (Table S1), electron microscopy study of materials (Figures S2−S4, Table S2), physisorption analysis (Figure S5, Table S3), TGA analysis (Figure S6, Table S4), IR spectra of material (Figure S7), bandgap determination (Figures S8 and S9, Table S5), XPS analysis (Table S6, Figures S10−S15), photocatalytic performance of the material (Figure S16 and S17, Tables S7−S9), analysis of the material after reaction (Table S10, Figures S18−S20), and DFT theoretical modeling and simulations (Figures S21−S28, Table S11) (PDF)

■ AUTHOR INFORMATION

Corresponding Authors

Igor Djerdj − *Department of Chemistry, Josip Juraj Strossmayer University of Osijek, Osijek HR-31000, Croatia;* ⓘ orcid.org/0000-0002-0646-4928; Email: igor.djerdj@kemija.unios.hr

András Sápi − *Department of Applied and Environmental Chemistry, University of Szeged, Szeged H-6720, Hungary;* ⓘ orcid.org/0000-0001-6557-0731; Email: sapia@chem.us-zeged.hu

Authors

Dalibor Tatar − *Department of Chemistry, Josip Juraj Strossmayer University of Osijek, Osijek HR-31000, Croatia*

Habib Ullah − *Department of Engineering, Faculty of Environment, Science and Economy, University of Exeter, Cornwall TR10 9FE, United Kingdom;* ⓘ orcid.org/0000-0001-9290-0265

Mohit Yadav − *Department of Applied and Environmental Chemistry, University of Szeged, Szeged H-6720, Hungary*

Jelena Kojčinović − *Department of Chemistry, Josip Juraj Strossmayer University of Osijek, Osijek HR-31000, Croatia;* ⓘ orcid.org/0000-0003-1420-0380

Stjepan Šarić − *Department of Chemistry, Josip Juraj Strossmayer University of Osijek, Osijek HR-31000, Croatia*

Imre Szenti − *Department of Applied and Environmental Chemistry, University of Szeged, Szeged H-6720, Hungary*

Tina Skalar − *Faculty of Chemistry and Chemical Technology, University of Ljubljana, Ljubljana SI-1000, Slovenia*

Matjaž Finšgar − *Faculty of Chemistry and Chemical Engineering, University of Maribor, Maribor SI-2000, Slovenia;* ⓘ orcid.org/0000-0002-8302-9284

Mi Tian − *Department of Engineering, Faculty of Environment, Science and Economy, University of Exeter, Cornwall TR10 9FE, United Kingdom;* ⓘ orcid.org/0000-0001-6983-6146

Ákos Kukovecz − *Department of Applied and Environmental Chemistry, University of Szeged, Szeged H-6720, Hungary;* ⓘ orcid.org/0000-0003-0716-9557

Zoltán Kónya − *Department of Applied and Environmental Chemistry, University of Szeged, Szeged H-6720, Hungary;* ⓘ orcid.org/0000-0002-9406-8596

Complete contact information is available at:
https://pubs.acs.org/10.1021/acsami.4c00478

Author Contributions

The manuscript was written through contributions of all authors. All authors have given approval to the final version of the manuscript.

Notes

The authors declare no competing financial interest.

■ ACKNOWLEDGMENTS

■ REFERENCES

(1) Jiang, X.; Nie, X.; Guo, X.; Song, C.; Chen, J. G. Recent Advances in Carbon Dioxide Hydrogenation to Methanol via Heterogeneous Catalysis. *Chem. Rev.* **2020**, *120* (15), 7984−8034.

(2) Wang, Y.; Winter, L. R.; Chen, J. G.; Yan, B. CO_2 hydrogenation over Heterogeneous Catalysts at Atmospheric Pressure: From Electronic Properties to Product Selectivity. *Green Chem.* **2021**, *23* (1), 249−267.

(3) Kong, T.; Jiang, Y.; Xiong, Y. Photocatalytic CO_2 conversion: What Can. We Learn from Conventional CO_X hydrogenation? *Chem. Soc. Rev.* **2020**, *49* (18), 6579−6591.

(4) Ulmer, U.; Dingle, T.; Duchesne, P. N.; Morris, R. H.; Tavasoli, A.; Wood, T.; Ozin, G. A. Fundamentals and Applications of Photocatalytic CO_2 Methanation. *Nat. Commun.* **2019**, *10* (1), 1−12.

(5) Chung, C. H.; Tu, F. Y.; Chiu, T. A.; Wu, T. T.; Yu, W. Y. Critical Roles of Surface Oxygen Vacancy in Heterogeneous Catalysis over Ceria-Based Materials: A Selected Review. *Chem. Lett.* **2021**, *50* (5), 856−865.

(6) Zhang, Y.; Yang, X.; Yang, X.; Duan, H.; Qi, H.; Su, Y.; Liang, B.; Tao, H.; Liu, B.; Chen, D.; et al. Tuning Reactivity of Fischer−Tropsch Synthesis by Regulating TiO_x Overlayer over Ru/TiO_2 Nanocatalysts. *Nat. Commun.* **2020**, *11* (1), 3185.

(7) Morris, A. J.; Meyer, G. J.; Fujita, E. Molecular Approaches to the Photocatalytic Reduction of Carbon Dioxide for Solar Fuels. *Acc. Chem. Res.* **2009**, *42* (12), 1983−1994.

(8) Li, X.; Yu, J.; Jaroniec, M. Hierarchical Photocatalysts. *Chem. Soc. Rev.* **2016**, *45* (9), 2603−2636.

(9) Wang, K.; Lu, J.; Lu, Y.; Lau, C. H.; Zheng, Y.; Fan, X. Unravelling the C−C Coupling in CO_2 Photocatalytic Reduction with H_2O on Au/TiO_{2-x}: Combination of Plasmonic Excitation and Oxygen Vacancy. *Appl. Catal. B Environ.* **2021**, *292*, 120147.

(10) Li, K.; Peng, B.; Peng, T. Recent Advances in Heterogeneous Photocatalytic CO_2 Conversion to Solar Fuels. *ACS Catal.* **2016**, *6* (11), 7485−7527.

(11) Crake, A.; Christoforidis, K. C.; Godin, R.; Moss, B.; Kafizas, A.; Zafeiratos, S.; Durrant, J. R.; Petit, C. Titanium Dioxide/Carbon Nitride Nanosheet Nanocomposites for Gas Phase CO_2 Photoreduction under UV-Visible Irradiation. *Appl. Catal. B Environ.* **2019**, *242*, 369−378.

(12) Jiang, H.; Katsumata, K. I.; Hong, J.; Yamaguchi, A.; Nakata, K.; Terashima, C.; Matsushita, N.; Miyauchi, M.; Fujishima, A. Photocatalytic Reduction of CO_2 on Cu_2O-Loaded Zn-Cr Layered Double Hydroxides. *Appl. Catal. B Environ.* **2018**, *224*, 783−790.

(13) Akrami, S.; Murakami, Y.; Watanabe, M.; Ishihara, T.; Arita, M.; Fuji, M.; Edalati, K. Defective High-Entropy Oxide Photocatalyst with High Activity for CO_2 Conversion. *Appl. Catal. B Environ.* **2022**, *303*, 120896.

(14) Sarkar, A.; Wang, Q.; Schiele, A.; Chellali, M. R.; Bhattacharya, S. S.; Wang, D.; Brezesinski, T.; Hahn, H.; Velasco, L.; Breitung, B. High-Entropy Oxides: Fundamental Aspects and Electrochemical Properties. *Adv. Mater.* **2019**, *31*, 26.

(15) Rost, C. M.; Sachet, E.; Borman, T.; Moballegh, A.; Dickey, E. C.; Hou, D.; Jones, J. L.; Curtarolo, S.; Maria, J.-P. Entropy-Stabilized Oxides. *Nat. Commun.* **2015**, *6* (1), 8485.

(16) Amiri, A.; Shahbazian-Yassar, R. Recent Progress of High-Entropy Materials for Energy Storage and Conversion. *J. Mater. Chem. A* **2021**, *9* (2), 782−823.

(17) Chu, S.; Majumdar, A. Opportunities and Challenges for a Sustainable Energy Future. *Nature* **2012**, *488* (7411), 294−303.

(18) Chen, H.; Fu, J.; Zhang, P.; Peng, H.; Abney, C. W.; Jie, K.; Liu, X.; Chi, M.; Dai, S. Entropy-Stabilized Metal Oxide Solid Solutions as CO Oxidation Catalysts with High-Temperature Stability. *J. Mater. Chem. A* **2018**, *6* (24), 11129−11133.

(19) Zhang, Y.; Zhao, S.; Feng, J.; Song, S.; Shi, W.; Wang, D.; Zhang, H. Unraveling the Physical Chemistry and Materials Science of CeO_2-Based Nanostructures. *Chem* **2021**, *7* (8), 2022−2059.

(20) Aneggi, E.; Boaro, M.; De Leitenburg, C.; Dolcetti, G.; Trovarelli, A. Insights into the Redox Properties of Ceria-Based Oxides and Their Implications in Catalysis. *J. Alloys Compd.* **2006**, *408−412*, 1096−1102.

(21) Zhang, Y. -C.; Li, Z.; Zhang, L.; Pan, L.; Zhang, X.; Wang, L.; Fazal-E-Aleem; Zou, J. -J. Role of Oxygen Vacancies in Photocatalytic Water Oxidation on Ceria Oxide: Experiment and DFT Studies. *Appl. Catal. B Environ.* **2018**, *224*, 101−108.

(22) Nundy, S.; Tatar, D.; Kojčinović, J.; Ullah, H.; Ghosh, A.; Mallick, T. K.; Meinusch, R.; Smarsly, B. M.; Tahir, A. A.; Djerdj, I. Bandgap Engineering in Novel Fluorite-Type Rare Earth High-Entropy Oxides (RE-HEOs) with Computational and Experimental Validation for Photocatalytic Water Splitting Applications. *Adv. Sustain. Syst.* **2022**, *6* (7), 1−20.

(23) Tatar, D.; Kojčinović, J.; Marković, B.; Széchenyi, A.; Miletić, A.; Nagy, S. B.; Ziegenheim, S.; Szenti, I.; Sapi, A.; Kukovecz, Á.; et al. Sol-Gel Synthesis of Ceria-Zirconia-Based High-Entropy Oxides as High-Promotion Catalysts for the Synthesis of 1,2-Diketones from Aldehyde. *Molecules* **2021**, *26* (20), 6115.

(24) Kojčinović, J.; Sahu, M.; Hajra, S.; Tatar, D.; Klaser, T.; Skoko, Ž.; Jagličić, Z.; Sadrollahi, E.; Litterst, F. J.; Kim, H. J.; et al. Nanocrystalline Triple Perovskite Compounds $A_3Fe_2BO_9$ (A = Sr, Ba; B = W, Te) with Ferromagnetic and Dielectric Properties for Triboelectric Energy Harvesting. *Mater. Chem. Front.* **2022**, *6* (9), 1116−1128.

(25) Hartman, P.; Chan, H. K. Application of the Periodic Bond Chain (PBC) Theory and Attachment Energy Consideration to Derive the Crystal Morphology of Hexamethylmelamine. *Pharm. Res. An Off. J. Am. Assoc. Pharm. Sci.* **1993**, *10* (7), 1052−1058.

(26) Bijelić, J.; Stanković, A.; Medvidović-Kosanović, M.; Marković, B.; Cop, P.; Sun, Y.; Hajra, S.; Sahu, M.; Vukmirović, J.; Marković, D.; et al. Rational Sol-Gel-Based Synthesis Design and Magnetic, Dielectric, and Optical Properties Study of Nanocrystalline $Sr_3Co_2WO_9$ Triple Perovskite. *J. Phys. Chem. C* **2020**, *124* (23), 12794−12807.

(27) Rodríguez-Carvajal, J. Recent Advances in Magnetic Structure Determination by Neutron Powder Diffraction. *Phys. B Phys. Condens. Matter* **1993**, *192* (1−2), 55−69.

(28) Momma, K.; Izumi, F. VESTA: A Three-Dimensional Visualization System for Electronic and Structural Analysis. *J. Appl. Crystallogr.* **2008**, *41* (3), 653−658.

(29) Schneider, C. A.; Rasband, W. S.; Eliceiri, K. W. NIH Image to ImageJ: 25 Years of Image Analysis. *Nat. Methods* **2012**, *9* (7), 671−675.

(30) Smidstrup, S.; Markussen, T.; Vancraeyveld, P.; Wellendorff, J.; Schneider, J.; Gunst, T.; Verstichel, B.; Stradi, D.; Khomyakov, P. A.; Vej-Hansen, U. G.; et al. QuantumATK: An Integrated Platform of Electronic and Atomic-Scale Modelling Tools. *J. Phys.: condens. Matter* **2020**, *32* (1), 015901.

(31) Klechkovskaya, V. V.; Imamov, R. M. Electron Diffraction Structure Analysis (from Vainshtein to Our Days). *Crystallogr. Rep.* **2001**, *46* (4), 534−549.

(32) Mikhaylov, R. V.; Nikitin, K. V.; Glazkova, N. I.; Kuznetsov, V. N. Temperature-Programmed Desorption of CO_2, Formed by CO Photooxidation on TiO_2 Surface. *J. Photochem. Photobiol. A Chem.* **2018**, *360*, 255−261.

(33) Lima, J. R. D. O.; Ghani, Y. A.; Da Silva, R. B.; Batista, F. M. C.; Bini, R. A.; Varanda, L. C.; De Oliveira, J. E. Strontium Zirconate Heterogeneous Catalyst for Biodiesel Production: Synthesis, Characterization and Catalytic Activity Evaluation. *Appl. Catal. A Gen.* **2012**, *445−446*, 76−82.

(34) Guo, M.; Lu, J.; Wu, Y.; Wang, Y.; Luo, M. UV and Visible Raman Studies of Oxygen Vacancies in Rare-Earth-Doped Ceria. *Langmuir* **2011**, *27* (7), 3872−3877.

(35) Yu, K.; Qiu, X.; Xu, X.; Wei, W.; Peng, B.; Zhou, Z. Enhanced Photoluminescence of Nd2O3 Nanoparticles Modified with Silane-Coupling Agent: Fluorescent Resonance Energy Transfer Analysis. *Appl. Phys. Lett.* **2007**, *90* (9), 2−5.

(36) Câmara, J. G.; da Silva, D. M.; Kassab, L. R. P.; Silva-Neto, M. L.; Palacios, G.; de Araújo, C. B. Random Lasing and Replica Symmetry Breaking in GeO_2-PbO-MgO Glass−Ceramics Doped with Neodymium. *Sci. Rep.* **2022**, *12* (1), 1−12.

(37) Rahimi-Nasrabadi, M.; Pourmortazavi, S. M.; Aghazadeh, M.; Ganjali, M. R.; Sadeghpour Karimi, M.; Novrouzi, P. Samarium Carbonate and Samarium Oxide; Synthesis, Characterization and Evaluation of the Photo-Catalytic Behavior. *J. Mater. Sci.: mater. Electron.* **2017**, *28* (7), 5574−5583.

(38) Ortega, P. P.; Hangai, B.; Moreno, H.; Rocha, L. S. R.; Ramírez, M. A.; Ponce, M. A.; Longo, E.; Simões, A. Z. Tuning Structural, Optical, and Gas Sensing Properties of Ceria-Based Materials by Rare-Earth Doping. *J. Alloys Compd.* **2021**, *888*, 161517.

(39) Meijer, J. M.; Aarts, L.; Van Der Ende, B. M.; Vlugt, T. J. H.; Meijerink, A. Downconversion for Solar Cells in YF₃: Nd³⁺, Yb³⁺. *Phys. Rev. B - Condens. Matter Mater. Phys.* **2010**, *81* (3), 1−9.

(40) Wang, C.; Zhang, T.; Pan, X. Potential of Visible and Near-Infrared Reflectance Spectroscopy for the Determination of Rare Earth Elements in Soil. *Geoderma* **2017**, *306* (July), 120−126.

(41) Shaw, M.; Samanta, D.; Bera, S.; Mahto, M. K.; Salam Shaik, M. A.; Konar, S.; Mondal, I.; Dhara, D.; Pathak, A. Role of Surface Oxygen Vacancies and Oxygen Species on CuO Nanostructured Surfaces in Model Catalytic Oxidation and Reductions: Insight into the Structure-Activity Relationship Toward the Performance. *Inorg. Chem.* **2022**, *61* (37), 14568−14581.

(42) Yttrium - XPS Thermofisher scientific

(43) Mullins, D. R.; Overbury, S. H.; Huntley, D. R. Electron Spectroscopy of Single Crystal and Polycrystalline Cerium Oxide Surfaces. *Surf. Sci.* **1998**, *409* (2), 307−319.

(44) Romeo, M.; Bak, K.; El Fallah, J.; Le Normand, F.; Hilaire, L. XPS Study of the Reduction of Cerium Dioxide. *Surf. Interface Anal.* **1993**, *20* (6), 508−512.

(45) Borchert, H.; Frolova, Y. V.; Kaichev, V. V.; Prosvirin, I. P.; Alikina, G. M.; Lukashevich, A. I.; Zaikovskii, V. I.; Moroz, E. M.; Trukhan, S. N.; Ivanov, V. P.; et al. Electronic and Chemical Properties of Nanostructured Cerium Dioxide Doped with Praseodymium. *J. Phys. Chem. B* **2005**, *109* (12), 5728−5738.

(46) Xia, P.; Antonietti, M.; Zhu, B.; Heil, T.; Yu, J.; Cao, S. Designing Defective Crystalline Carbon Nitride to Enable Selective CO₂ Photoreduction in the Gas Phase. *Adv. Funct. Mater.* **2019**, *29* (15), 1900093.

(47) Liu, Z.; Menéndez, C.; Shenoy, J.; Hart, J. N.; Sorrell, C. C.; Cazorla, C. Strain Engineering of Oxide Thin Films for Photocatalytic Applications. *Nano Energy* **2020**, *72*, 104732.

(48) Ahmetović, S.; Vasiljević, Z.; Rajić, V.; Bartolić, D.; Novaković, M.; Tadić, N. B.; Cvjetićanin, N.; Nikolić, M. V. Examination of the Doping Effects of Samarium (Sm³⁺) and Zirconium (Zr⁴⁺) on the Photocatalytic Activity of TiO₂ Nanofibers. *J. Alloys Compd.* **2023**, *930*, 167423.

(49) Zhao, Z.; Liu, J.; Sa, G.; Xu, A. Electronic Properties and Photodegradation Ability of Nd-TiO₂ for Phenol. *J. Rare Earths* **2022**, *40* (7), 1063−1072.

(50) Yaqoob, A. A.; Noor, N. H. B. M.; Serrà, A.; Ibrahim, M. N. M. Advances and Challenges in Developing Efficient Graphene Oxide-Based Zno Photocatalysts for Dye Photo-Oxidation. *Nanomaterials* **2020**, *10* (5), 932.

(51) Li, P.; Chen, X.; Li, Y.; Schwank, J. W. A Review on Oxygen Storage Capacity of CeO₂ -Based Materials: Influence Factors, Measurement Techniques, and Applications in Reactions Related to Catalytic Automotive Emissions Control. *Catal. Today* **2019**, *327*, 90−115.

(52) Sun, Y.; Li, C.; Djerdj, I.; Khalid, O.; Cop, P.; Sann, J.; Weber, T.; Werner, S.; Turke, K.; Guo, Y.; et al. Oxygen Storage Capacity versus Catalytic Activity of Ceria-Zirconia Solid Solutions in CO and HCl Oxidation. *Catal. Sci. Technol.* **2019**, *9* (9), 2163−2172.

(53) Boaro, M.; Colussi, S.; Trovarelli, A. Ceria-Based Materials in Hydrogenation and Reforming Reactions for CO₂ Valorization. *Front. Chem.* **2019**, *7*, 28.

(54) Trovarelli, A. Catalytic Properties of Ceria and CeO₂-Containing Materials. *Catal. Rev.: sci. Eng.* **1996**, *38* (4), 439−520.

(55) Chang, K.; Zhang, H.; Cheng, M. J.; Lu, Q. Application of Ceria in CO₂ Conversion Catalysis. *ACS Catal.* **2020**, *10* (1), 613−631.

(56) Álvarez, A.; Borges, M.; Corral-Pérez, J. J.; Olcina, J. G.; Hu, L.; Cornu, D.; Huang, R.; Stoian, D.; Urakawa, A. CO₂ Activation over Catalytic Surfaces. *ChemPhyschem* **2017**, *18* (22), 3135−3141.

(57) Etim, U. J.; Zhang, C.; Zhong, Z. Impacts of the Catalyst Structures on CO₂ Activation on Catalyst Surfaces. *Nanomaterials* **2021**, *11* (12), 3265.

(58) Sarkar, A.; Loho, C.; Velasco, L.; Thomas, T.; Bhattacharya, S. S.; Hahn, H.; Djenadic, R. Multicomponent Equiatomic Rare Earth Oxides with a Narrow Band Gap and Associated Praseodymium Multivalency. *Dalt. Trans.* **2017**, *46* (36), 12167−12176.

(59) Djenadic, R.; Sarkar, A.; Clemens, O.; Loho, C.; Botros, M.; Chakravadhanula, V. S. K.; Kübel, C.; Bhattacharya, S. S.; Gandhi, A. S.; Hahn, H. Multicomponent Equiatomic Rare Earth Oxides. *Mater. Res. Lett.* **2017**, *5* (2), 102−109.

(60) Shangguan, W.; Liu, Q.; Wang, Y.; Sun, N.; Liu, Y.; Zhao, R.; Li, Y.; Wang, C.; Zhao, J. Molecular-Level Insight into Photocatalytic CO₂ Reduction with H₂O over Au Nanoparticles by Interband Transitions. *Nat. Commun.* **2022**, *13* (1), 1−11.

(61) Zhao, J.; Yang, Q.; Shi, R.; Waterhouse, G. I. N.; Zhang, X.; Wu, L. Z.; Tung, C. H.; Zhang, T. FeO−CeO₂ Nanocomposites: An Efficient and Highly Selective Catalyst System for Photothermal CO₂ Reduction to CO. *NPG Asia Mater.* **2020**, *12* (1), 5.

(62) Pu, Y.; Li, W.; Cai, Y.; Wei, X.; Wang, X.; Chen, C.; Zou, W.; Dong, L. Effects of different treatment atmospheres on CeO₂/g-C₃N₄ photocatalytic CO₂ reduction: good or bad? *Catal. Sci. Technol.* **2021**, *11*, 2827−2833.

(63) Rajkumar, T.; Sápi, A.; Ábel, M.; Kiss, J.; Szenti, I.; Baán, K.; Gómez-Pérez, J. F.; Kukovecz, Á.; Kónya, Z. Surface Engineering of CeO₂ Catalysts: Differences Between Solid Solution Based and Interfacially Designed Ce₁−ₓMₓO₂ and MO/CeO₂ (M = Zn, Mn) in CO₂ Hydrogenation Reaction. *Catal. Lett.* **2021**, *151* (12), 3477−3491.

(64) Cheng, Z.; Lo, C. S. Mechanistic and Microkinetic Analysis of CO₂ Hydrogenation on Ceria. *Phys. Chem. Chem. Phys.* **2016**, *18* (11), 7987−7996.

(65) Wang, X.; Shi, H.; Kwak, J. H.; Szanyi, J. Mechanism of CO₂ Hydrogenation on Pd/Al₂O₃ Catalysts: Kinetics and Transient DRIFTS-MS Studies. *ACS Catal.* **2015**, *5* (11), 6337−6349.

(66) Guo, Y.; Mei, S.; Yuan, K.; Wang, D. J.; Liu, H. C.; Yan, C. H.; Zhang, Y. W. Low-Temperature CO₂ Methanation over CeO₂-Supported Ru Single Atoms, Nanoclusters, and Nanoparticles Competitively Tuned by Strong Metal-Support Interactions and H-Spillover Effect. *ACS Catal.* **2018**, *8* (7), 6203−6215.

(67) Lin, L.; Yao, S.; Liu, Z.; Zhang, F.; Li, N.; Vovchok, D.; Martínez-Arias, A.; Castaneda, R.; Lin, J.; Senanayake, S. D.; et al. In Situ Characterization of Cu/CeO₂ Nanocatalysts for CO₂ Hydrogenation: Morphological Effects of Nanostructured Ceria on the Catalytic Activity. *J. Phys. Chem. C* **2018**, *122* (24), 12934−12943.

(68) László, B.; Baán, K.; Varga, E.; Oszkó, A.; Erdőhelyi, A.; Kónya, Z.; Kiss, J. Photo-Induced Reactions in the CO₂-Methane System on Titanate Nanotubes Modified with Au and Rh Nanoparticles. *Appl. Catal. B Environ.* **2016**, *199*, 473−484.

(69) Sápi, A.; Halasi, G.; Kiss, J.; Dobó, D. G.; Juhász, K. L.; Kolcsár, V. J.; Ferencz, Z.; Vári, G.; Matolin, V.; Erdöhelyi, A.; et al. In Situ DRIFTS and NAP-XPS Exploration of the Complexity of CO₂ Hydrogenation over Size-Controlled Pt Nanoparticles Supported on Mesoporous NiO. *J. Phys. Chem. C* **2018**, *122* (10), 5553−5565.

(70) Goguet, A.; Meunier, F. C.; Tibiletti, D.; Breen, J. P.; Burch, R. Spectrokinetic Investigation of Reverse Water-Gas-Shift Reaction Intermediates over a Pt/CeO₂ Catalyst. *J. Phys. Chem. B* **2004**, *108* (52), 20240−20246.

(71) Ferencz, Z.; Erdo, A.; Baa, K.; Oszko, A.; O, L.; Kiss, J.; Papp, C.; Steinrück, H.-P.; Kiss, J. Effects of Support and Rh Additive on Co-Based Catalysts in the Ethanol Steam Reforming Reaction. *ACS Catal.* **2014**, *4*, 1205−1218.